Department of Chemistry

University of Helsinki

Finland

Structural characterisation via C-14-PMMA impregnation technique: Method and application development

Juuso Sammaljärvi

Academic Dissertation

To be presented, with permission of the Faculty of Science of the University of Helsinki, for public examination in lecture hall A110, Department of Chemistry, on 8 December 2017, at 12 noon.

Supervisors

University lecturer Marja Siitari-Kauppi, PhD

Department of Chemistry

University of Helsinki

Helsinki, Finland

Manager Jean-Claude Parneix, PhD

Etudes Recherches Materiaux

Poitiers, France

Pre-examiners

Professor Carl-Eric Wilen

Åbo Akademi

Turku, Finland

Privatdozent Urs Mäder

Universität Bern

Bern, Switzerland

Opponent

Dr. Stephane Gaboreau

French Geological Survey

Orleans, France

ISSN 0358-7746

ISBN 978-951-51-3707-4 (paperback)

ISBN 978-951-51-3708-1 (PDF)

Unigrafia

Helsinki 2017

Ihminen lannistaa pimeyden, hän tutkii kaiken pohjia myöten, tutkii kallion pimeät uumenet.

Job 28:3

Acknowledgements

The work presented here was carried out between 2010 and 2017 at the University of Helsinki and received funding from the EU POSINAM project, Posiva Oy, Doctoral School of Nuclear Engineering and Radiochemistry (YTERA) and the CHEMS Chemistry and Molecular Sciences Doctoral School (CHEMS) at the University of Helsinki.

I would like to thank my supervisor Marja Siitari-Kauppi for her supervision and guidance throughout this period. My fellow PMMA group members (Jussi Ikonen, Mikko Voutilainen, Jukka Kuva, Eveliina Muuri, Xiaodong Li, Hanna Aromaa and Eini Puhakka) have also been extremely helpful during this journey. In particular, I would like to thank Jussi Ikonen, with whom I have carried out much of the experimental work described herein. I also thank my colleagues Heini Ervanne and Hanna Aromaa with whom I have shared office space. My thanks also go to Professor Jukka Lehto and the other members of the Radiochemistry Unit for creating such a fine workplace environment.

In addition, I would like to thank Dr Karl-Heinz Hellmuth for his invaluable help extended throughout my work on this thesis project as well as for the treasure trove of literature he provided. I cannot help but admire his scientific zeal and determination. I extend my gratitude to Paul Sardini and Jean-Claude Parneix as well for their help and guidance during my time in Poitiers, France. I am indebted to all those in Poitiers with whom I worked and spent time. I would like to thank Philippines, Emilie and Alexandre from the Institut de Radioprotection et de Sûreté Nucléaire (IRSN) for their fruitful cooperation. I also thank Antero Lindberg for his geological expertise, and Bo Johanson and Sari Lukkari from the Geological Survey of Finland for their assistance with the scanning electron microscopy (SEM) analyses. Furthermore, I thank the two pre-examiners of this thesis for their valuable input, and Vanessa Fuller for assistance with the English-language revisions.

Finally, I thank my parents, my sister and her family for their support and encouragement throughout my dissertation work. My dearest father in particular provided his theoretical physicist's point of view on my publications. And, ultimately, I thank my wife Charlotta for her unwavering support.

Helsinki, 2017

Juuso Sammaljärvi

Abstract

The C-14 polymethyl methacrylate (C-14-PMMA) impregnation technique is used to analyse the spatial distribution of porosity. As such, this work focuses on two interlinked aims: to further develop the C-14-PMMA impregnation technique, particularly the polymerisation and autoradiography steps; and to further develop its application extending it from granitic materials to fine-grained structures such as clays as well.

To achieve these aims, method development focused on making the C-14-PMMA impregnation technique more flexible and suitable to a wide variety of conditions while maintaining its robustness. As such, we investigated the use of thermally degrading initiators and other impregnants. Thus, we examined the use of thermally degrading initiators as a way of completing the entire sample handling procedure in a laboratory without necessitating transportation to irradiation facilities, which are currently rare. Furthermore, we studied the use of a water-soluble comonomer, 2-hydroxyethyl methacrylate (HEMA), to allow for the possibility of impregnating water-saturated matrices in future.

The second aim focused on the application-related development for the C-14-PMMA impregnation technique and tailoring the methodology to suit the different applications. Towards this end, we compared our results with those obtained via previously used methodologies and other measurement techniques. As such, the C-14-PMMA impregnation technique can be linked to multiple other techniques, providing comprehensive information on the materials studied. In this study, we examined the mineral porosities of rock at the centimetre scale using C-14-PMMA autoradiography (AG) and at the micrometre scale using scanning electron microscopy (SEM) imaging with the aim of studying the effect of the mineral structure on the spatial distribution of porosity. We also studied the fixation of a contrast agent that does not require pressurised intrusion used to image the connected porosity of crystalline rock through SEM and X-ray tomography. In this case, impregnation with methyl methacrylate (MMA) served to fix the contrast agent in place.

Our results from the method development studies show that polymerisation can be reliably accomplished within crystalline rock using thermally degrading initiators with no notable drawbacks. We also found that clay rock could be impregnated and the impregnant could be polymerised with the same initiators as well. The two-monomer mixtures (100% C-14-labelled

methyl methacrylate (C-14-MMA) and a mixture of 75% HEMA and 25% C-14-MMA) yielded fairly similar results and were consistent with reference values. The application development studies show that valuable information may be gained by combining the spatial distribution of the porosity with spatial information on the minerology. The contrast agent for SEM and X-ray tomography was successfully fixed in place by impregnation and polymerisation, and the contrast improved through both imaging techniques.

List of original publications

This dissertation is based on research described in the following articles, referred to herein by their Roman numerals:

I Sammaljärvi J., Jokelainen L., Ikonen J., Siitari-Kauppi M. 2012. *Free radical polymerisation of MMA with thermal initiator in brick and Grimsel granodiorite*, Engineering Geology, 135-136, 52–59.

II Sammaljärvi J., Shroff Rama M., Ikonen J., Muuri E., Hellmuth K.-H., Siitari-Kauppi M. 2016. *Free radical polymerisation of methacrylates with thermal initiator in clay rock*, Engineering Geology, 210, 70–83.

III Sammaljärvi J., Lindberg A., Voutilainen M., Kuva J., Ikonen J., Johanson B., Siitari-Kauppi M., Pitkänen P., Koskinen L. 2017. *Multi-scale study of the mineral porosity of veined gneiss and pegmatitic granite from Olkiluoto, Western Finland*, Journal of Radioanalytical and Nuclear Chemistry (DOI: 10.1007/s10967-017-5530-5)

IV Kuva J., Sammaljärvi J., Parkkonen J., Siitari-Kauppi M., Lehtonen M., Turpeinen T., Timonen J. 2017. Voutilainen M., *Imaging connected porosity of crystalline rock by contrast agent-aided X-ray microtomography and scanning electron microscopy*, Journal of Microscopy (DOI: 10.1111/jmi.12661)

Contributions to the publications:

In article I, I developed the experimental set-up, performed the experiments, performed all analyses in the article and wrote the draft.

In article II, I developed the experimental setup, carried out the C-14-PMMA autoradiography and performed most of the SEM/energy dispersive X-ray spectroscopy (EDS) analyses and half of the thermogravimetric analyses (TGAs) described in the article. I also wrote the draft.

In article III, I completed the C-14-PMMA impregnations and porosity measurements using AG and the SEM-EDS analyses described in the article. I also wrote the draft.

In article IV, I participated in the sample preparation, the SEM-EDS analyses and their interpretation and participated in writing the manuscript.

List of abbreviations

2D	Two-dimensional
3D	Three-dimensional
AG	Autoradiography
AIBN	Azobisisobutyrnitrile
C-14-MMA	C-14-labelled methyl methacrylate
C-14-PMMA	C-14 polymethyl methacrylate
BPO	Benzoyl peroxide
BSE	Backscattered electron
CHEMS	Chemistry and Molecular Sciences Doctoral School
CsCl	Caesium chloride
DI	Diffusion in situ Experiment
EB	Electron beam
EDS	Energy dispersive X-ray spectroscopy
FESEM	Field emission scanning electron microscopy
FIB	Focused ion beam
GPC	Gel permeation chromatography
H-3-MMA	Tritium-labelled methyl methacrylate
HEMA	2-hydroxyethyl methacrylate
IRSN	Institut de Radioprotection et de Sûreté Nucléaire
IUPAC	International Union of Pure and Applied Chemistry
KBS-3	Kärnbränslesäkerhet concept
LTD	Long-Term Diffusion Experiment
LTDE-SD	Long-Term Sorption Diffusion Experiment
MMA	Methyl methacrylate
NMR	Nuclear magnetic resonance
PEG	Polyethylene glycol
PMMA	Polymethyl methacrylate
POSINAM	Pore Space Investigation in Natural and Artificial Materials
QWBA	Quantitative whole-body autoradiography
REPRO	Retention properties
SE	Secondary electron
SEM	Scanning electron microscopy
STED	Stimulated emission depleted microscopy
TGA	Thermogravimetric analysis
TDE	Through Diffusion Experiment
UV	Ultraviolet
WPDE	Water-Phase Diffusion Experiment
XRD	X-ray powder diffraction
YTERA	Doctoral School of Nuclear Engineering and Radiochemistry

Table of contents

1. Introduction

Bedrock is composed of porous stone, consisting of numerous grains of various minerals featuring pores both within and outside these grains. These pores represent the empty space within the rock. In most cases, water can intrude into this empty space. The path the water travels is often a tortuous labyrinth because the pores are unevenly distributed spatially, including some paths which are dead ends. Similarly, some pores are wide while others are narrow. This pore network traverses grains of different sizes and of differing chemical compositions. Compounds dissolved in water can also interact with the rock. Because of these features, the porosity considerably influences a given material's mechanical strength and water conductivity along with other parameters. This holds true not just for rocks, but also for building materials and soils for instance. In turn, this influences the usefulness of a given material, whether that material is used to build a house or to host a spent nuclear fuel repository. Because porosity influences many important aspects of a material, it is not always sufficient to simply know the total porosity. As such, we must also identify the pore structure and its spatial distribution.

This calls for structural characterisation of a given material. Structural characterisation often represents the sum of work across several techniques, where one technique provides results regarding one parameter and another yields results related to another. Together, a picture of the entire material emerges. As such, the C-14 polymethyl methacrylate (C-14-PMMA) impregnation technique was developed to deliver quantitative information on the spatial distribution of the porosity on a hand-specimen scale. Different materials and varied conditions, however, call for adjustments to measurement techniques in order to deliver optimal results. Technology related to porosity measurements also continues to undergo development, whereby keeping abreast of such developments remains important. Hence, the driving force behind this work focused on developing the C-14-PMMA impregnation technique, making use of the latest technological developments. Furthermore, this work focuses on method development allowing completion of the entire procedure in a laboratory setting without necessitating the use of irradiation facilities to complete tracer fixation. In addition, our efforts also focused on widening the synergy obtainable by using complementary characterisation techniques. This broadens the scope of possible applications.

In this work, I first present the background concerning porosity, its measurement and significance, followed by an overview of the experimental details, plans and the characterisation techniques used throughout this work. Next, I present the results along with a discussion of their implications. Finally, I provide the conclusions from this work and the future outlook related to these findings.

2. Background

2.1. The porosity of geological materials

Porosity is the void space within a given sample, the exact form and nature of which depends on the specific material. Porosity represents an important property of geological materials. Furthermore, porosity controls the fluid flow and transport through geological formations, and acts as an interface between circulating solutions and the reactive mineral phases (Norton & Knapp, 1977). In addition, porosity controls fluid storage in aquifers, oil and gas fields as well as geothermal systems. Porosity also acts as a link between the properties of individual minerals and the bulk properties of the rock (Anovitz & Cole, 2015). While porosity may comprise only 1% or less of the material, it can profoundly affect the properties of the rock (Sprunt & Brace, 1974).

Total porosity can be divided into connected and unconnected porosities. As such, connected porosity is composed of those pores accessible to fluids or gases. By contrast, unconnected pores are not in contact with other pores. That is, they can contain stagnant fluids or gases. Pores can also be divided along different criteria. In terms of geometry, porosity falls into pores that are fairly round and into fissures that are long and narrow. Transgranular fissures transect several mineral grains. Yet, intergranular pores and fissures are found around mineral grains, which are also called grain boundary pores. In addition, intragranular pores and fissures are located inside mineral grains. When the grain is composed of distinct lamellae, this porosity can be called interlamellar porosity (Kuva et al., 2015). Such pores can be connected to transgranular or intergranular pores or be isolated (Siitari-Kauppi, 2002).

The aperture of porosity covers several magnitudes of scale from nanometres to hundreds of centimetres. International Union of Pure and Applied Chemistry (IUPAC) terminology divides pores based on aperture into macropores (>50 nm), mesopores (2–50 nm) and micropores (<2 nm). No single method adequately covers all scales; therefore, different techniques must be used for different scales (Anovitz & Cole, 2015). In crystalline rock, porosity can be divided into micropores, where diffusion represents the main transportation phenomenon, and into fractures, where the main transportation phenomenon is flow (Mazurier et al., 2016).

In crystalline rock, the porosity is the sum of cracks, joints, fissures, grain boundaries and pores (Norton & Knapp, 1977). In sedimentary rock, the porosity is the space between particles, the

interlayers in swelling clays, cracks and the stacking faults in the structure (Velde & Meunier, 2008). In a given geological material, primary porosity typically originates from the crystallisation of the melt (Petford & McCaffrey, 2003) or the sedimentation process (Anovitz & Cole, 2015). Porosity resulting from the crystallisation of the melt develops as the result of physical and chemical processes. For instance, cooling magma can contain large amounts of volatile species that escape, leaving behind empty cavities, cavities which are often interconnected. As such, extrusive rock cools relatively quickly, leaving little time for crystallisation. Therefore, extrusive rock typically features a small grain size and sometimes fails to crystallise at all. In the formation of extrusive rock, planar contacts between lava flows result in continuous porous zones, while discontinuous columnar joints develop as the magma cools layer by layer. During the formation of intrusive rock, the cooling of magma is slower, whereby coarse grains develop and porosity results from fracturing during this process. The porosity distribution in rocks is composed of roughly equally sized grains (equigranular), differing from those displaying a porphyritic grain size distribution characterised by early-formed large grains surrounded by a more fine-grained matrix. In this kind of porphyritic rock, porosity concentrates around the smallest and largest grain sizes, while in more equigranular rocks, the porosity is more evenly distributed (Petford & McCaffrey, 2003). Furthermore, the temperature gradient between the intruding magma and the surrounding host rock affects the development of cooling joints. As such, the steeper the thermal gradient, the more intensive the joint formation. The composition of the magma influences the temperature of the magma, whereby mafic magmas are hotter than felsic magmas. The initial composition of the magma also plays a role in the formation of secondary porosity since rocks borne of mafic magma crystallise into minerals more susceptible to secondary porosity formation than those borne of felsic magma.

Sedimentary rocks are formed by the sedimentation of the weathering products of igneous rock, metamorphic rock and other sedimentary rocks. The nature of these sedimentary components affects the evolution of porosity from the initial sedimentation through to diagenesis and other possible processes. Depending on the main components of the sediment, the resulting rock can be, for example, carbonate rock, sandstone or mudstone. In sedimentary rocks, the shape, sorting and packing of the grains exert a major effect on the porosity and pore structure. In sandstones, much of the initial porosity can be intergranular

porosity (Kyser, 2000; Zinszner & Pellerin, 2007), while in carbonate rock, the primary porosity is more heterogeneous (Kyler, 2000; Mazzullo, 2004). In addition, the primary intergranular porosity in sedimentary rocks is a function of sorting (Lucia, 2007). Yet, poorly sorted sandstone features a lower porosity than well-sorted sandstone; but, poorly sorted carbonate rock can be more porous than well-sorted carbonate rock. The primary porosity in carbonate rocks is also influenced by the particles deposited. These particles can feature porosity within them. In addition, fenestral pores form from gas bubbles and sediment shrinkage. In reefs, shelter and growth-framework pores result from the reef build-up (Mazzullo, 2004). In addition, the porosity typically increases with a smaller grain size, although theoretically this is not necessary. However, packing and sorting are often imperfect and can become even more imperfect with processes leading to smaller-sized grains.

As such, this porosity can then be modified by numerous mechanisms, such as deformation, metamorphism, hydrothermal alteration, diagenesis and weathering. The porosity produced by these secondary processes is known as secondary porosity (Anovitz & Cole, 2015). Secondary porosity develops via the formation of cracks, fractures and fissures produced where local stress exceeds the local strength. This local stress can be augmented by twin lamellae interactions, kink bands, deformation lamellae and stress concentrations at the grain boundary contacts and around intracrystalline cavities. Thus, local strength may be weaker near cleavage planes, along grain boundaries and along the internal surface produced by the water–rock interaction. Fractures can then result from the coalescence of several microcracks (Kranz, 1983).

Diagenesis is the process following the sedimentation of weathering products and is strongly influenced by the composition of the sediment (Kyler, 2000). Cementation of small particulate matter into the intergranular space of the sediment decreases the porosity, as does an increasing compaction during burial. Furthermore, packing grains into a denser arrangement caused by compaction reduces the porosity. In turn, compaction further results in grain rotation, deformation and eventually breakage, thereby reducing the porosity (Kyler, 2000). Compaction, however, also creates fractures, thus increasing porosity (Laubach & Ward, 2006). In addition, compaction produces a pressure solution with a high dissolved silica concentration in pore water and these resulting microenvironments consisting of highly dissolved silica become cementation sites. Other sources of silica cement may result from the

silica released from the feldspar breakdown and silica released during clay mineral diagenesis. If thorough cementation occurs early during the burial process, this may provide a rigid framework preventing further compaction. Clay minerals in the matrix of sandstone or carbonate stone become deformed and compressed during compaction, causing the plugging of the pore throats. A similar decrease in porosity is observed for clay-rich mudstone. With an increasing strain resulting from compaction, the porosity decreases and the pore throats narrow (Dewhurst et al., 1998), while simultaneously creating pore elongation (Day-Stirrat et al., 2012). Furthermore, clay carried into this matrix from an outside source can carry differing effects depending on the clay mineral assemblage composition. For instance, kaolinite fillings fill pores, but tend to lower the permeability only moderately, while illite fillings decrease both the porosity and permeability dramatically (Kyler, 2000). Clay minerals can also coat the framework minerals, potentially hindering quartz cement nucleation and thus preserving porosity (Lai et al., 2017). Diagenesis of carbonate rock can increase or decrease porosity. As such, the diagenetic process that increases the porosity of carbonate rocks stems from the dissolution of carbonate minerals. This dissolution can act selectively on certain minerals or be nonselective resulting in different types of pore systems. Yet, the pores resulting from the dissolution of carbonate minerals can be subsequently filled by cementation, again decreasing the porosity. Both dissolution and cementation are influenced by the composition of the interacting fluid (Mazzullo, 2004).

In turn, the deformation behaviour of rock can be either brittle or ductile depending on the pressure and temperature conditions (Byerlee, 1968; Gowd & Rummel, 1980). In the case of brittle deformation, grains break resulting in intragranular and transgranular porosity. In ductile deformation, the pore space can collapse and minerals readjust becoming more densely packed. This behaviour is typical of, for example, sandstone at a high pressure (Gowd & Rummel, 1980). In addition, ductile deformation leads to folded structures (Bucher & Grapes, 2011). Thus, the presence of the initial porosity can affect the details of the transition from brittle to ductile deformation (Hirth & Tullis, 1989), and highly porous rocks can form deformation bands characterised by an enhanced cohesion and a reduced permeability (Fossen et al., 2007).

In a similar vein, metamorphism develops when the pressure and temperature of the rock increases causing the rock matter to reorganise. Therefore, metamorphism is often associated

with other processes such as deformation, and the presence of high-temperature fluids affect the metamorphic process. In addition, retrograde metamorphism results from the effect of a decreasing temperature and pressure. Both crystalline and sedimentary rock can experience metamorphism, and a metamorphic rock can re-experience metamorphism (Lehtinen et al., 1998). Some minerals are considered distinctly metamorphic in the sense that they form at an elevated temperature and are not found in diagenetically transformed sediments. High-temperature metamorphism can include the partial melting of a rock mass, producing migmatite rocks composed of metamorphic and igneous rock (Bucher & Grapes, 2011). These structures are typically highly banded and the porosity often displays a strong preferential direction. In addition, different kinds of metamorphism exist. For instance, regional metamorphism is associated with large-scale deformation in tectonic events. On a smaller scale, dynamic metamorphism is associated with fault zones. This kind of metamorphism typically occurs under a high pressure and a low temperature, and, therefore, only involves mechanical forces that cause the cracking and granulation of the rock matrix (Bucher & Grapes, 2011). This typically produces fine-grained structures (Bradbury et al. 2015) that can fill fractures caused by high pressure (Holland et al., 2006). Contact metamorphism, by contrast, results from a temperature increase caused by the intrusion of magma into cooler country rock. In brittle domains, the magma intrudes into preexisting fractures or fractures generated by the intrusion itself. In more ductile domains, the magma pushes aside the host rock developing a measure of schistosity (Kornprobst, 2002). In both cases, the resulting metamorphic rock is typically fine-grained (Bucher & Grapes, 2011). Finally, hydrothermal metamorphism results from the interaction of rock with a high-temperature fluid. This metamorphism is a type of hydrothermal alteration. Shock metamorphism is associated with meteorite impacts or violent volcanic eruptions.

Hydrothermal alteration refers to rock being in contact with high temperature aqueous solutions via the pore network. As such, hydrothermal alteration is often associated with diagenesis in sedimentary rocks and metamorphism in crystalline rocks. The alteration minerals resulting from hydrothermal alteration are often found along and adjacent to fractures. Furthermore, the assemblage of these alteration minerals can be uniform along the length of the fracture, but abruptly change tangentially to the fracture (Norton & Knapp, 1977). When several such fractures are closely spaced, overlapping alteration zones can form.

In turn, porosity can also be generated by the dissolution of the host rock (Jamtveit & Hammer, 2012; Emmanuel et al., 2015). Often, this dissolution is coupled to precipitation and together they form a replacement reaction (Jamtveit & Hammer, 2012; Putnis, 2015). In addition, some minerals are more prone to porosity formation than others. For instance, the Na-rich phase of alkali feldspar appears to be more prone to pore formation (Dultz, et al., 2006). Furthermore, a hydrothermal alteration can also result in the formation of secondary minerals such as sulphides, clay minerals and calcite. These and other minerals can be deposited in existing pore systems with varying consequences. As such, the deposition's effect could clog the pores caused by other metamorphic processes (Bucher & Grapes, 2011) or, in more limited cases, affect the permeability and porosity to some degree (Stack, 2015; Emmanuel et al., 2015). The hydrothermal alteration of plagioclase, for example, can lead to sericitisation (Que & Allen, 1996) or saussuritisation (Morad et al., 2009). Among these, clay minerals are fine-grained and, therefore, have an abundance of intergranular porosity. Overall, the trend in hydrothermal alteration tends towards the replacement of tectosilicates (quartz group, feldspars, plagioclases, etc.) with sheet silicates (clay minerals, mica, chlorites and serpentines).

By contrast, weathering results from the rock's exposure to the elements. For instance, rock in equilibrium within the lithosphere adapts to the new conditions prevalent on the Earth's surface. The primary varieties of weathering consist of chemical, mechanical and biological weathering (Uusinoka, 1983). For weathering to occur, the rock lies directly or connects to the external surface, while the pores are the medium through which internal weathering may also occur (Dultz, et al., 2006; Jamtveit & Hammer, 2012). Furthermore, weathering results in a high porosity and secondary minerals. Similar to a hydrothermal alteration associated with other processes, some minerals are more prone to weathering (Formoso, 2006). These secondary porosity processes can also clog pores with fillings (Jamtveit & Hammer, 2012), while the crystallisation of fillings generates volumetric stress causing cracking (Jamtveit et al., 2011). In crystalline rock in general, weathering appears to increase the apertures of microcracks leading to more macrocracks. In addition, intragranular porosity was found to increase in biotite and plagioclase minerals (Mazurier et al., 2016).

2.2. Observing porosity

Porosity measurement techniques often work via direct observation using radiation or through indirect observation through a liquid or gas interaction (Anovitz & Cole, 2015). Yet, different techniques work best at different scales and highlight different aspects of porosity. Furthermore, various techniques have different porosity and permeability ranges for optimal performance, while the types of artefacts differ as well (Hellmuth et al., 1995). Laboratory measurements can yield a bulk porosity reflecting the whole of the studied mass or yield spatially resolved information in two or three dimensions. Bulk measurements are most useful for homogeneous materials, but provide an incomplete set of information on samples with a heterogeneous distribution of porosity. In the spatially resolved measurements of porosity, challenges relate to the representativeness of the sample studied versus the bulk material. In addition, spatially resolved porosity measurements must take into account the resolution limits of the specific technique. For instance, if the resolution is too low to resolve the porous features, the pores might not be observed at all or the result will simply yield the bulk porosity of the given area. Typically, a higher resolution requires working with smaller samples, rendering the question of sample preparation and artefacts caused by prehandling even more important. As a result, it is prudent to subject the studied material to several different porosity measurement techniques.

The spatial distribution of porosity can be observed directly via microscopic techniques. Microscopic techniques provide information on both connected and unconnected porosity that can be distinguished from the studied sample surface. For example, optical light microscopy is traditionally applied to evaluate the pore system. To improve the contrast between pores, fractures and sound material, colourant or fluorescein-doped resins is allowed to intrude into the pore system. Minerals can also be stained to facilitate mineral assessment (Anovitz & Cole, 2015). Porosity on a micro-scale can be observed directly via scanning electron microscopy (SEM) (Sprunt & Brace, 1974; Anovitz & Cole, 2015). Direct observation of the porosity allows for characterisation of both connected and unconnected porosity. The determination of pores is typically achieved by segmenting and thresholding the microscopic images. This can be accomplished in three dimensions (3D) using the focused ion beam (FIB)/SEM method, where the sample surface is milled with fast ion bombardment and images are taken between the different milling steps. This FIB/SEM method can be used to produce

3D images of the material; with proper image handling, 3D porosity measurements become possible (Keller et al., 2011; 2013). The sample size here is only cubic micrometres and, therefore, more than one area is often measured to achieve representative results (Keller et al., 2013; Davy et al., 2017). Because of the small scales, however, electron microscopy is not well-suited for porosity measurements of centimetre-scale samples. In such cases, it is better to complement imaging with another porosity measurement technique.

Nuclear magnetic resonance (NMR) measurements, by contrast, provide core-scale porosity information. As such, NMR measures the response of hydrogen protons inside an external magnetic field. The response of hydrogen protons stems from the water or oil saturated in the rock. NMR relaxometry has been used to study the pore distribution of water-saturated compacted clay. It is based on measuring the relaxation times of ^{1}H nuclei of water molecules. The relaxation time depends on the local chemical environment and, in this case, whether the water lies in the interlayer pore space of the clay or in the non-interlayer pores (Ohkubo et al., 2016). When saturated samples are measured, the amplitude of the T_2 transverse relaxation is directly proportional to the porosity, while the decay rate is related to the pore size, fluid type and its viscosity in the pore space (Anovitz & Cole, 2015). Nuclei other than ^{1}H can also be used. In addition, xenon NMR measurements with a flow of ^{129}Xe through the reservoir rock measure effective porosity, permeability and tortuosity (Wang et al., 2005).

By contrast, positron emission tomography and neutron radiography have been used to characterise porosity in crystalline rock. This technique is based on following the annihilation radiation caused by the beta-plus emitter in the sample matrix (Degueldre et al., 1996).

X-ray microtomography is a noninvasive technique that measures porosity based on various X-ray attenuation factors of different phases which, in practise, correspond to density, allowing us to distinguish between minerals with different densities. A two-dimensional (2D) image of the sample is taken at each small increment of a rotational angle; from these 2D images, a 3D image of the sample structure can be constructed (Noiriel, 2015). For long samples, more than one set of 2D images may be required. Via image segmentation, the voxels are classified into pores and solids. Once this segmentation is completed, the data can be used to calculate the porosity and to study the pore geometry and the pore-space distribution. The resolution is defined by the voxel size, which typically depends on the sample size.

In addition, gas expansion and gas adsorption techniques are used to provide bulk porosity values. Gas expansion porosimetry works by allowing gas stored in a reference cell to isothermally expand into a sample cell. For instance, He gas is commonly used in gas expansion methods because its small size allows it to rapidly penetrate small pores, it is inert, is considered an ideal gas and has a high diffusivity enabling rapid intrusion into low permeability rock. In comparison, gas adsorption is used to characterise the pore surface area and volume. As such, N_2 gas is commonly used for gas adsorption studies. The pore aperture affects the adsorption isotherm patterns and, therefore, can be used to measure the type of dominant porosity aperture in the sample material (Anovitz & Cole, 2015). Yet, in samples with a low porosity and low connectivity, the results are less clear (Hellmuth et al., 1995).

Saturation methods using a wetting fluid provide bulk porosity weighting of the studied sample before and after saturation. Here, water represents the typical liquid used in saturation experiments, whereby this method is sometimes called water gravimetry (International Society for Rock Mechanics, 1979). Other liquids, such as toluene and dichloromethane, have also been used as well as synthetic groundwater with a composition similar to that found at the sampling site. Through-diffusion of a tracer-containing water solution can be used to investigate the effective porosity available to specific ions or compounds (van Loon et al., 2007; Glaus et al., 2010; Sevee, 2010). Furthermore, water titration of presaturated samples can be used to measure the connectedness of the pore system (Dultz et al., 2006). Saturation methods, however, remain challenging to apply to samples with small nm-sized pores or samples with a very low permeability (Anovitz & Cole, 2015). Fluids intruded into geomaterials can also be introduced via pressure. For example, mercury porosimetry, a well-established technique for measuring porosities, is based on intruding mercury into the porous space via a pressurised process. As such, mercury porosimetry provides information on the pore size distribution, the total porosity, the skeletal and apparent density and the specific surface area. Pores between 500 µm and 3.5 nm can be investigated and the pores must be connected (Giesche, 2006). As a method, however, mercury porosimetry is very sensitive to artefacts resulting from the sample preparation and measurement conditions (Hellmuth et al., 1995). Many porosity measurement techniques depend on or can be improved by impregnating the pore space either temporarily or permanently.

2.3. Impregnation

The pore space of a given material can be impregnated for various reasons. For instance, if the impregnant has a labelling property to it, it can be used to image the pore space. The sample treatment methodology depends on the sample material, but typically it should empty the pore space as much as possible since the portion not removed will be viewed as part of the mineral volume (Lucia, 2007). As a result, impregnation is normally carried out on dried samples. In this case, the pore space is free of both water and air which can inhibit or retard the full impregnation of the sample. In some cases, such as in situ experiments, this is difficult to achieve. Some materials also change their structure through drying. Thus, it might be necessary to perform a gradual solvent exchange or use a water-soluble impregnant (Rodgers, 2004).

The impregnant can contain a tracer compound that enhances the contrast compared to the rest of the matrix (Soeder, 1990; Baraka-Lokmane, 2002) or it can serve as a contrast agent itself (Klobes, et al., 1997a; Darot & Reuschle, 1999; Dultz et al., 2006). Yet another use is to harden a brittle or soft sample for other analyses. An impregnant can also be used to fix another type of marker compound in place (Degueldre et al., 1996). In geomaterials, impregnation is often carried out in a vacuum if possible without disturbing the pore structure. Thus, the aim typically focuses on highlighting or imaging the pore structure or yielding a better mechanical strength for the sample. Impregnation is also used in the conservation and consolidation of archaeological materials, such as limestone (De Witte et al., 1977; Bugani et al., 2007), wood and other organics (Rodgers, 2004) as well as for terracotta ceramics (Rodgers, 2004; Langhals & Oginski, 2008). In conservation efforts, the reversibility and the inertness of the filling consolidation material remain key parameters. Polyethylene glycol (PEG) is the most commonly used reversible consolidant (Rodgers, 2004), although other polymers such as different acrylates (Langhals & Oginski, 2008; Bugani et al., 2007) and fluoroelastomers and alkylalkoxysilane oligomers have also been used (Bugani et al., 2007). In certain media, such as water-logged wood, PEG's use has proven problematic. Therefore, studies have focused on alternative consolidant materials such as natural polymers (Walsh, et al., 2014; 2017).

The intrusion of organic monomers into porous materials can be used to influence the properties of the resulting composite material. In this case, the porous material is commonly

called a ‘substrate’, which accepts the impregnant into its structure. Impregnating monomers into a substrate to form composites or to influence the properties of the resulting polymer have been widely studied (Gao, 2004; Priya Dasan, 2015). These composites are composed of the polymer chains placed between the clay layers and the clay layers themselves. They can be prepared either by intruding or mixing a ready-made polymer into the clay interlayer space or by polymerising a monomer intruded into the interlayer space of the clay material. Furthermore, the composites can be made either by intercalation or exfoliation. Intercalated structures preserve the original layered structure of the clay, while exfoliation involves individual clay layers being separated from each other and then randomly dispersed in the polymer matrix (Zeng & Lee, 2001; Priya Dasan, 2015). A common trait in these composites is that the clay substrate is modified to increase the compatibility with the hydrophobic monomer, such as methyl methacrylate (MMA) (Zeng & Lee, 2001; Wang et al., 2002; Liu et al., 2003; Zhang et al., 2003; Tsai et al., 2010).

Depending upon the specific case, it might be desirable to have the impregnant in such a state that it can be removed later if necessary (Rodgers, 2004). In some cases, hysteresis during intrusion and extrusion exists, and this can be used to gain new information (Giesche, 2006). In other cases, however, maintaining the impregnant within the sample is desirable, whereby its removal is not planned. In addition, different methods of fixing the impregnant in place exist. In the case of Wood’s metal, simply cooling the sample saturated with Wood’s metal causes the molten metal to solidify. In the case of monomer impregnants, free-radical polymerisation can be used. Geomaterials have been studied via impregnation using mercury as a part of a mercury porosimetry measurement. The mercury trapped in the pores was located using X-ray micro-computed tomography (Klobes, et al., 1997a; Klobes, et al., 1997b). Wood’s metal is another impregnant that has been used to fill the pore space for enhanced contrast in the study of cements (Willis et al., 1998; Abell et al., 1999), coal (Pyrak-Nolte et al., 1995; Pyrak-Nolte et al., 1997; Dultz et al., 2006), clay rock (Desbois et al., 2016) and feldspar grains (Dultz et al., 2006). Furthermore, a combination of mercury and Wood’s metal impregnation has been used to characterise different aspects of cement porosity (Kaufmann, 2009) and mudstone porosity (Hildenbrand & Urai, 2003; Klaver et al., 2015). The pore space can also be visualised with the aid of resins containing fluorescein (Soeder, 1990). Beyond

mercury and Wood's metal, the pore space can also be highlighted with the aid of radioactive tracers, while the pore space can be visualised using autoradiography (AG).

2.4. Autoradiography (AG)

Autoradiography (AG) is based on measuring the radiation coming from within a sample. Some of the first radioactivity measurements were completed using AG. For instance, the first application dating to 1867, occurred when Niepce de St. Victor recorded the blackening of silver chloride and iodide emulsions using uranium nitrate and tartrate (Rogers, 1967). In addition, Becquerel determined the radioactivity of uranium through photography in 1896 (Rogers, 1967). Thus, AG initially served as a way of imaging the radioactivity naturally present in a sample material, soon evolving to include radioactive tracers deliberately placed in the samples.

The primary modes of interaction using radiation depend on whether the radiation is charged or uncharged. An alfa particle has a positive charge and a characteristic energy (Knoll, 2010), attracting orbital electrons and repulsing other atomic nuclei near it. Alfa particles lose energy quickly along a typically straight path. Due to the quick energy loss, the trace left by the alfa particle is strong but highly localised (Rogers, 1967). In contrast, beta particles are electrons with a nuclear origin and, unlike alfa particles, have a continuum of energies since the energy is shared between the beta particle and the antineutrino particle produced by the beta-minus decay (Knoll, 2010). By virtue of its negative charge, the beta particle repulses other electrons and, therefore, may knock electrons out of their orbits. Furthermore, the beta particles will lose energy in this interaction and change course. A beta particle can also lose energy by passing close to an atomic nucleus, resulting in a Bremsstrahlung interaction. These varied interactions cause the beta radiation to produce much longer and more complicated tracks in AG (Rogers, 1967). Due to the varying energy distributions, the range also varies. Electrons produced by the internal conversion mechanism behave similarly to beta particles, although their initial energy is well-defined instead of falling along a continuum. Positrons produced by beta-plus radiation lose energy in the buffetings by orbital electrons, although the tail end of a positron track differs as it annihilates in a collision with an orbital electron.

Uncharged radiation, such as neutrons, X-rays and gamma rays, is more challenging to image using AG since it requires direct collision with electrons or nuclei. These collisions are fairly unlikely, translating into the long range without interactions. Gamma rays produce infrequent secondary electrons, which may produce tracks similar to beta particles. Yet, AG is sufficiently sensitive for these types of radiation and produces blackening in experiments (Forberg, et al., 1964).

Many parameters affect the resolution of AG (L'Annuziata, 2003; Sardini, et al., 2006, Siitari-Kauppi et al., 1998). Resolution is defined as the distance that must separate the two objects before they can be distinguished from each other. In terms of the source of the activity, the primary factors affecting the resolution consist of the isotope choice, the distance between the source and film and the sample thickness. The lower the maximum energy of the isotopes, the shorter the distance the emitted particle travels. As the emitted particle travels a certain distance, a part of the emission originates from within the sample and not simply from the surface. This broadens the specific feature on AG. Therefore, the best resolution can be achieved using radionuclides with the lowest maximum energies. If the distance between the source and the film increases, the resolution decreases quickly (Siitari-Kauppi, et al., 1998). In essence, this means that the AG samples should be well-polished so that the distance the emitted particles travel is consistent across the sample surface. If a good polish is not achieved, the resulting AG will be blurry (Siitari-Kauppi, et al., 1998). Furthermore, an increasing sample thickness tends to decrease the resolution. Yet, a sample thinner than the effective range of the emitter will suffer from a loss of quantitativity.

Quantitative AG measurements have been completed on a microscopic scale by counting under a microscope the developed grains or the tracks produced by the emitted particles (Rogers, 1967). On the macroscopic scale, calculations of the optical densities are more practical, developing into an approach widely used since the advent of computerised densitometry (Palacios et al., 1981). In order to make these kinds of quantitative measurements, calibration standards must be integrated into each exposure. As such, a standard series of known activities can be used to plot the function of the optical density of the imaging film and the activity (L'Annunziata, 2003; Solon, 2015). These standards are often plastic containing the studied nuclide (Treutler & Freyer, 1984; Geary, et al., 1985), although they can also consist of the sample material such as tissue impregnated with a known quantity

of activity (Unnerstall, et al., 1982). Both types of standards can yield similar results with the same isotope (Davenport & Hall, 1988), but calibrating the sample containing one nuclide with the standard of another nuclide can be difficult for some isotopes, including using a ^{14}C standard for ^{3}H samples (Geary et al., 1985) and using a ^{14}C standard for ^{32}P (Miller, 1991). Yet, other combinations may work quite well, such as using a ^{14}C standard for ^{125}I (Miller & Zahniser, 1987; Baskin & Wimpy, 1989) or a ^{14}C standard for ^{35}S (Miller, 1991).

The mechanism producing autoradiographic images depends on the method used. Traditional film AG is based on reducing silver atoms within a silver-halide grain of the film emulsion, yielding a latent image (Rogers, 1967; L'Annunziata, 2003). Different films are optimised for different isotopes. For example, single-coated films, containing one emulsion layer (e.g., Kodak BioMax MR), are optimised for direct-exposure techniques with low-energy radioisotopes (e.g., ^{14}C, ^{35}S and ^{33}P) (Siitari-Kauppi, 2002). The latent image is revealed by the development of the film, yielding a reduction of all silver atoms in the silver-halide crystal into metallic silver, forming a visible black dot. A single hit by a particle is sufficient to convert the silver-halide grain into a developable state, such that local blackening of the film is directly proportional to the local activity (L'Annunziata, 2003). The developed film is then scanned with a flatbed scanner or another digitation mode for further analysis. Film AG has a rather good sensitivity and good resolution, particularly for low-energy radionuclides. It also provides flexibility in terms of the exposure time given that latent image fading is typically quite slow. The exposure, however, can also be rather too long. In addition, film AG has a rather limited linear dynamic range. Thus, some more highly active areas might be oversaturated, while areas of lesser activity lie along the linear region of the optical densities. Therefore, a balance must be struck between the resolution and quantitativity. This is typically found only by trial and error.

Storage phosphor screen imaging, a more recent method of producing autoradiographic images, relies on the interaction of particles with a photostimulable phosphor screen that contains $BaFBr:Eu^{2+}$ crystals. The energy of the radiation converts Eu^{2+} to Eu^{3+}, liberating electrons to the conduction band of the phosphor crystals. These electrons are then trapped in bromine vacancies in the structure. These vacancies serve a similar purpose to the latent image silver halides of film AG. Exposure to stimulating laser light of 633 nm releases the trapped electrons from the bromine vacancies back to the conduction band of the crystals and

converts Eu^{3+} back to Eu^{2+}. This process releases 390-nm photons, which are collected in a photomultiplier tube (L'Annunziata, 2003). Phosphor screen–based AG has a higher sensitivity and a larger linear dynamic range than film AG (L'Annunziata 2003; Kämäräinen et al., 2006; Sardini et al., 2015), allowing imaging of low- and high-activity areas using the same exposure with a higher certainty. In addition, phosphor screen AG represents a sensitive method, typically producing images through shorter exposures than film AG. Furthermore, phosphor screen–imaging plates are reusable following erasure through bright-light exposure requiring no development chemicals, rendering this a slightly simpler setup than film AG. Yet, while the imaging plates are reusable, artefacts tend to accumulate over time. While the linear dynamic range is larger when using phosphor screen AG than through film AG, it remains limited and the exposure time must be chosen carefully. As such, imaging plates are also affected by the signal fade, which limits the maximal exposure time considerably. This may be important in low-activity samples.

Another method which performs AG through the direct measurement of radioactivity, called electronic AG, is based on multiple gas proportional counters in parallel (Donnard, et al., 2009a). Here, particles emitted from a sample pass through the protective window, enter the nearest microchannel and ionise the gas mixture. The resulting electrons are accelerated and collected. This system provides direct nuclear count data without necessitating a procedure for scanning films or imaging plates. Measurements based on electronic AG tend to be fast with a large linear dynamic range. In addition, the resolution depends on the detector design (L'Annunziata, 2003) and improvements to the detector design result in a resolution close to the limit imposed by the radiation range (Donnard et al., 2009b). While many applications of electronic AG use beta radiation, it is also suitable for alfa measurements (Sardini, et al., 2016).

The isotope used depends on the application. If the resolution is the only criteria, then the lowest energy isotope remains the best choice. Other criteria for the beta source might include an isotope that diffuses into certain areas of the sample matrix. The beta source can also be attached to a suitable compound. In this case, the affinities of the isotope are less important, while the properties of the compound become more important.

Many applications of AG lie in the field of biological sciences. The isotopes typically used in this field include ^{3}H, ^{14}C, ^{35}S and ^{125}I. Isotopes such as ^{11}C, ^{18}F, ^{22}Na and ^{90}Y may also be used (Solon et al., 2010). The internal conversion and Auger electron-emitting nuclides such as ^{55}Fe,

^{85}Sr, ^{109}Cd and ^{125}I have been used in various studies (Forberg, et al., 1964). In studies of drug distribution, two larger trends revolve around quantitative whole-body AG (QWBA) and cellular level microautoradiography (Solon, 2015). In QWBA, the compound studied is administered to a test animal, which is then euthanised. The carcass is quickly frozen, dehydrated and cryosectioned into 20- to 50-µm-thick slices. These slices are then mounted onto phosphor imaging plates. QWBA provides tissue-specific activity distributions with minimal disruption. In addition, QWBA represents a major step forward from the previous methodology of liquid scintillation counting from tissue homogenates. By contrast, microautoradiography proceeds with the compound studied being administered to the animal, which is then euthanised, followed by the sampling of tissue and organs. These samples are frozen, cryosectioned and placed on microscope slides pre-coated with a nuclear emulsion sensitive to the radiation emitted by the compound studied. This procedure uses traditional X-ray films developed in a darkroom (Solon, 2015).

AG has been used in the evaluation of tritium contamination in buildings scheduled for dismantling (Fichet et al., 2012). Another example of the use of AG in contaminant studies lies in the study of the uptake of ^{14}C by root vegetables (Ogiyama, et al., 2009). Here, comparison AG was also completed using ^{22}Na.

In geological studies, applications have often related to naturally occurring radionuclides (Rufer & Preusser, 2009; Sardini et al., 2016; Hellmuth et al., 2017) and the study of water–rock interactions, such as sorption. The use of AG in the study of sorption of ^{233}U and ^{241}Am from the Nevada Test Site in to different natural materials (alluvium, argillite, granite and tuff) found onsite was evaluated (Thompson & Wolfsberg, 1979). A radiolabelled tracer can be intruded into the sample material and will diffuse and sorb into minerals that have an affinity to this tracer. Such interactions occur via porous pathways within the rock. The sorption caesium on tonalite and mica gneiss was studied by examining the distribution of ^{134}Cs on thin slices via AG (Siitari-Kauppi et al., 1999). While sorption itself can be studied with AG, a typical use for AG focuses on obtaining information on the porous pathways that facilitate sorption and transport processes (Siitari-Kauppi, 2002). One field where this is specifically studied is the final deposition of spent nuclear fuel.

2.5. The final disposal of spent nuclear fuel

Spent nuclear fuel is a complex material. While primarily composed of uranium oxide, it also consists of transuranium elements and fission products of varying half-lives. In the event of canister failure, the instantaneous release fraction of spent nuclear fuel will consist of volatile elements such as Xe, Kr, I, Cs and Cl. A long-term release fraction, by contrast, primarily consists of uranium and transuranium elements (Ewing, 2015).

Plans are in place to deposit spent nuclear fuel from Finnish power plants in a deep geological repository in Olkiluoto, Western Finland (Posiva, 2012). Sweden (SKB, 2010a) and France (Andra, 2005) have also selected sites for their deep geological repositories. Different rock types characterise the selection of the potential disposal sites ranging from clay (Grambow, 2016), crystalline rock (Posiva, 2012; Hedin & Olsson, 2016; Laberov et al., 2016), salt rock (von Berlepsch & Haverkamp, 2016) and tuff (Swift & Bonano, 2016). Similar plans at various stages are also underway in countries such as Belgium (ONDRAF/NIRAS, 2011), Switzerland (SFOE, 2008), the United Kingdom (DECC, 2014) and Japan (NUMO, 2013). In Finland and Sweden, deposition is planned based on the Kärnbränslesäkerhet (KBS-3) concept (Posiva, 2010; SKB, 2010a; SKB, 2010b). According to this concept, multiple barriers prevent the entry of radionuclides into the biosphere. First, these barriers consist of the fuel rods and bundles themselves. The spent nuclear fuel is inserted into cast-iron inserts surrounded by copper canisters. The copper canisters are inserted into placements in tunnels, where they are surrounded by a bentonite buffer. The tunnels are backfilled and 400 metres of bedrock act as the final barrier against entry into the biosphere (SKB, 2010b; Posiva 2014a; Poteri, et al., 2014). The tunnels are closed after being backfilled. Most radionuclides in spent nuclear fuel are embedded in a ceramic matrix (UO_2) resistant to dissolution under the expected repository conditions. The canister ensures the prolonged containment of the spent nuclear fuel based on the mechanical strength of the cast-iron insert and the corrosion resistance of the copper overpack. The bentonite buffer separates the canisters from the host rock and contributes to maintaining conditions favourable to the integrity of the canister. The tunnel backfill limits and retards the release of radionuclides in the event of canister failure and contributes to the mechanical stability of the rock adjacent to the deposition tunnels. In the case of failure of the engineered barrier systems, the bedrock continues to retard and limit the transport of radionuclides. In addition, the host rock isolates the repository from the surface environment

and limits the possibility of intrusion. The placement of the deposition holes is set such that they do not cross-sect with any deformation zones (Poteri, et al., 2014). The closure of the tunnels prevents underground openings from compromising the long-term isolation of the repository from the surface environment. Closure also limits and retards the inflow of water and the release of radionuclides from the repository (Posiva, 2014a). Figure 1 illustrates the KBS-3 concept.

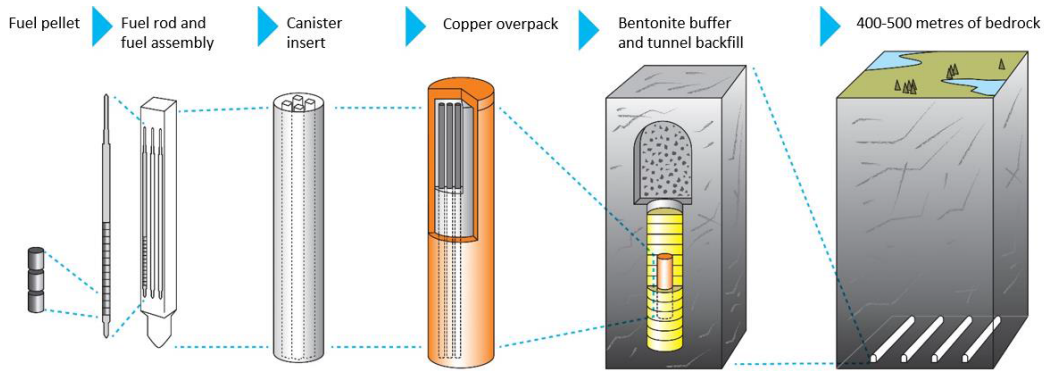

Figure 1. Illustration of the KBS-3 concept. Image adapted from Posiva Oy.

Safety case analysis (Poteri, et al., 2014) for the final deposition depends on many parameters related to the performance of the engineered barrier systems in the near-field and the properties of the geological formation in the far-field. Both short-term (Gaucher & Blanc, 2006) and long-term experiments (Gaboreau et al., 2011; Mäder et al., 2017) have examined the interface between man-made barriers and the host rock. The characteristics of the local geology affect the long-term storage of spent nuclear fuel and the mobility of the released radionuclides (Bradbury & Green, 1986). Furthermore, the porosity and its spatial distribution influence the retention of radionuclides in the pore space of the bedrock by acting as an interface between the radionuclides dissolved in the groundwater and the rock minerals. It is expected that the mineral composition and the pore structure will affect the diffusion of the radionuclides via various retention mechanisms such as diffusion into the matrix porosity (Voutilainen, et al., 2013; Sammaljärvi, et al., 2014; Sammaljärvi, et al., 2017; Voutilainen, et al., 2017a, Voutilainen, et al., 2017b).

Several long-term in situ experiments exist, such as the Long-Term Sorption Diffusion Experiment (LTDE-SD) in Sweden (Widestrand et al., 2007 & 2010), the Water-Phase Diffusion Experiment (WPDE) and the Through Diffusion Experiment (TDE) in Finland (Voutilainen et al., 2014), the Diffusion in situ Experiment (DI Experiment) at the Mont Terri Site in Switzerland (Palut et al., 2003) and the Long-Term Diffusion Experiment (LTD) at the Grimsel Test Site also in Switzerland (Soler et al., 2015), which studied the sorption and transport properties of different host rock systems. The sorption properties of important nuclides have also been studied in laboratory experiments (Byegård et al., 1998; García-Gutíerrez et al., 2006; C.A.J. Appelo et al., 2010; Muuri et al., 2016a; 2016b). The matrix diffusion in Kuru Grey granite has been studied using tracer experiments supported by rock matrix characterisation (Hölttä et al., 2007). In addition, granite from Palmottu has also been studied to ascertain the presence of precipitated uranium in the pore system (Kemppainen et al., 2001). Furthermore, the sorption of radionuclides into fractured granite with illite fillings was studied using groundwater solutions spiked with ^{137}Cs, ^{147}Pm, ^{241}Am and ^{90}Sr (Kamineni, et al., 1986).

Due to the varied effect that porosity plays on the safety of the final deposition, it is necessary to know more than just the bulk porosity. With knowledge of the spatial distribution of the porosity and connectivity, more realistic safety case calculations can be made. As such, the C-14-PMMA impregnation technique provides information on the spatial distribution of porosity.

3. The C-14-PMMA impregnation technique

C-14-PMMA AG is based on measuring the radiation resulting from the C-14-labelled tracer compound within the rock (Hellmuth, et al., 1993; Hellmuth, et al., 1994). The sample is first dried and then impregnated with a tracer solution of C-14-labelled methyl methacrylate (C-14-MMA). This tracer intrudes into the sample's connected porosity. Once the tracer has intruded into all accessible pore spaces, the tracer is fixed in place by polymerising it. When the tracer has been polymerised, the sample can be sawed, polished and placed on an autoradiographic film for film AG or on an imaging plate for digital AG. Figure 2 illustrates this procedure.

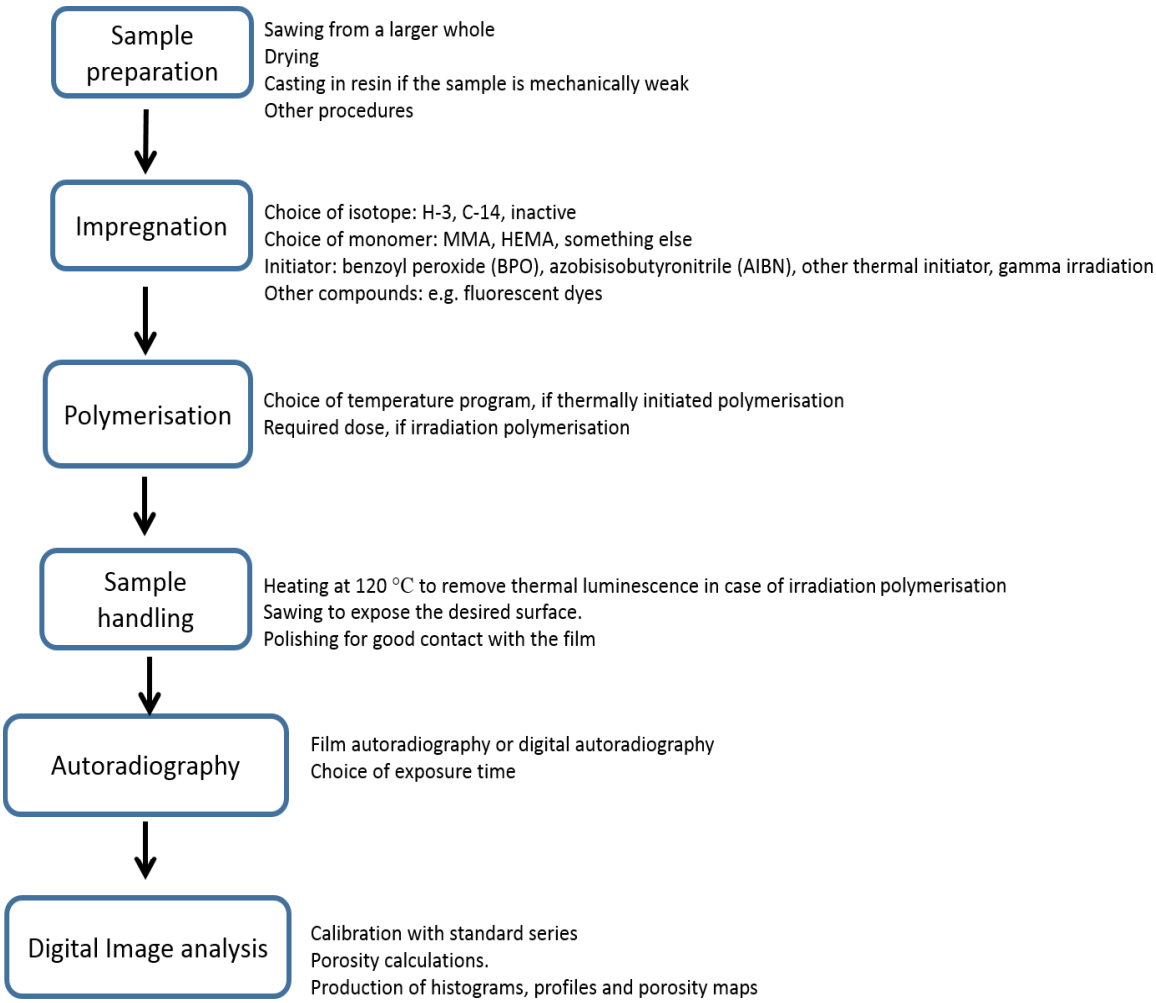

Figure 2. Procedural flow of the C-14-PMMA impregnation technique. Details of each step and the choices made during those steps detailed on the right.

The specific activity of the tracer is chosen based on the studied range of the porosity in mind (Hellmuth et al., 1993). For unaltered crystalline rocks with a low porosity of about 1% or less (Skagius & Neretnieks, 1985; Siitari-Kauppi, 2002), high activities such as 280 kBq/ml (Voutilainen, et al., 2008) or even 925 kBq/ml (Hellmuth, et al., 1994) should be used. For highly porous stones with a porosity of more than 1%, such as altered crystalline rocks (Norton & Knapp, 1977; Siitari-Kauppi, 2002; Kuva et al., 2012) or sedimentary rocks (Lucia, 2007; Zinszner & Pellerin, 2007), low specific activities such as 74 kBq/ml (Sammaljärvi, et al., 2016)

can be sufficient. If the tracer was polymerised using gamma irradiation, the thermoluminescence caused by the irradiation must be taken into account during the measurement procedure (Hellmuth, et al., 1993).

3.1. Experimental methods in the C-14-PMMA impregnation technique

3.1.1. Impregnants

Several aspects must be considered when choosing the impregnant. It needs to be non-reactive with mineral phases, polymerisable through common free-radical polymerisation methods within the sample (Hellmuth & Siitari-Kauppi, 1990) and the resulting polymer must be mechanically rigid and stable against radiolysis. The viscosity and the contact angle should be sufficiently similar to water, such that it can mimic the intrusion of water into geomaterials and perform rapid and complete impregnation (Hellmuth et al., 1993; Hellmuth et al., 1994). The tracer should not boil at low temperatures and should be non-toxic to facilitate safe handling. Methyl methacrylate (MMA) (shown in Figure 3) possesses these characteristics. As such, MMA represents the most common impregnant used in the C-14-PMMA impregnation technique and polymerises into polymer polymethyl methacrylate (PMMA), giving the technique its name. While MMA is more organophilic than hydrophilic, it is still sufficiently polar that it can enter into the small aperture interlamellar space of clays, into which more aliphatic monomers such as styrene and isoprene cannot enter (Blumstein, 1965). Styrene has been tested for use in this impregnation technique, but its low rate of radical formation results in unfeasibly long polymerisation times (Hellmuth et al., 1993).

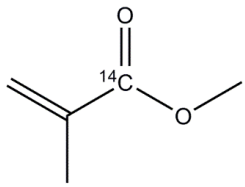

C-14-labelled methyl methacrylate

Figure 3. Chemical structure of methyl methacrylate (MMA)

In the C-14-MMA compound used in these experiments, the carbonyl carbon is labelled as C-14. The label, therefore, lies within the side group of the resulting polymer. C-14 is a low-energy beta emitter with a maximum energy of 156 keV and a half-life of 5360 years. The low-beta energy results in a short range and in optimal conditions, allowing for distances of 20 µm to be resolved using the AG method. The long half-life of the isotope allows for stockage maintenance for fairly long periods of time since the activity decays slowly and the specific activity can be low enough that there is only a small risk of autopolymerisation.

However, for specific purposes, other impregnants can be used. ^{3}H-labelled MMA (H-3-MMA) has been used in some applications to provide a better autoradiographic resolution owing to its short range due to its low beta energy of 18 keV. The short range of ^{3}H means that a resolution of 10 µm can be achieved, which is notably better than the resolution of 20 µm obtained using ^{14}C (Siitari-Kauppi et al., 1998; Hellmuth et al., 1999; Gaboreau et al., 2011; Robinet et al., 2015). One drawback from using H-3-MMA, however, results from its lower beta energy (18 keV), whereby higher specific activities must be used. Another drawback results from the short half-life, meaning solutions cannot be stored for as long as C-14-MMA solutions. The higher specific activity also increases the chance of autopolymerisation. Other uses for other impregnants lie in, for example, making the impregnant solution more water-soluble. Fluorescent dyes can also be mixed with the monomer to enhance the contrast in possible microscopic imaging and to label specific solutions for easy identification (Lähdemäki, et al., 2007; Hellmuth et al., 2011).

3.1.2. Polymerisation

The polymerisation of MMA is most commonly achieved via the free-radical polymerisation mechanism, although anionic polymerisation of MMA is also possible (Odian, 2004). MMA is a versatile monomer whose free-radical polymerisation can be initiated using several different techniques, such as the use of thermal initiators (Odian, 2004), redox initiators (Kotlík et al., 1980), irradiation with ionising radiation (Siitari-Kauppi, 2002), photoinitiation (Günzler et al., 2009) and ultrasonication (Gu et al., 2001). Free-radical polymerisation, in general, is initiated by reactive species R·, where the notation · denotes a radical species, produced from initiator compound I (Odian, 2004):

$$I \rightarrow R\cdot \quad \{1\}$$

The reactive species produced then reacts with monomer M by adding itself via the opening of the π bond to form new reactive centre $M_1\cdot$. This process is then repeated several times:

$$R\cdot + M \rightarrow M_1\cdot \quad \{2a\}$$

$$M_1\cdot + M \rightarrow M_2\cdot \quad \{2b\}$$

$$M_2\cdot + M \rightarrow M_3\cdot \quad \{2c\}$$

In general, this propagation reaction can be presented as

$$M_n\cdot + M \rightarrow M_{n+1}\cdot \quad \{3\}$$

The propagating polymer chain stops growing at some point and terminates. This can happen via combination, as

$$M_n\cdot + M_m\cdot \rightarrow M_{n+m} \quad \{4a\}$$

or via disproportionation, as

$$M_n\cdot + M_m\cdot \rightarrow M_n + M_m \quad \{4b\}$$

In general, the termination reaction can be expressed as

$$M_n\cdot + M_m\cdot \rightarrow dead\ polymer \quad \{5\}$$

In addition to the reaction series of initiation, propagation and termination, other reactions might occur. The most important of these other reactions consists of the chain transfer and the inhibition/retardation reactions. In the chain transfer, the radical centre is transferred from a growing chain to another atom species, such as a monomer, initiator, solvent compound or another polymer chain. This reaction can be presented as

$$M_n\cdot + XA \rightarrow M_n - X + A\cdot \quad \{6\}$$

where XA is the chain transfer agent and X is the transferred species. The radical produced in this reaction can then reinitiate the polymerisation. As the chain transfer leads to the premature termination of a growing chain, the observed molar masses are lower than what might be deduced from the extent of normal termination reactions {4a} and {4b}. The effect

on the polymerisation rate depends on how reactive produced radical A· is compared to the original propagating radical.

Aside from the chain transfer reactions, reactions with retarders or inhibitors might also occur. The distinction is determined by the strength of the effect. Their reaction can be generalised as

$$M_n \cdot + Z \rightarrow M_n + Z \cdot \text{ and/or } M_n Z \cdot \quad \{7\}$$

where Z is the inhibitor or retarder. Here, Z acts either by adding itself into the propagating chain or chain transfer to produce new radical Z· and a dead polymer chain. Regardless, the resulting radical species is usually considerably less reactive than the original propagating radical. Inhibitor compounds are typically added to commercial monomers to prevent autopolymerisation during storage and shipment. Another common inhibitor is atmospheric oxygen, which reacts with radicals to form rather unreactive peroxy compounds (Barnes, 1945).

A dead polymer no longer partakes in propagation reactions and, therefore, stops growing. The dead polymer is the normal end state in free radical polymerisation, although with living free radical polymerisation techniques, a system with little to no termination can be achieved. Depending on the technique, this can be achieved by including a reversible deactivation reaction such as that in nitroxide-mediated radical polymerisation (Grubbs, 2011) and atom transfer radical polymerisation (Matyjaszewski, 2012) or through a reversible chain transfer reaction as in the radical addition/fragmentation transfer (Moad et al., 2013).

Polymerisation within impregnated rock samples requires that initiation extends throughout the sample. This can be achieved by using a penetrating initiator or mixing the initiator into the feed monomer. The polymer product must be durable enough that it does not escape from the pores during subsequent sample handling involving sawing and polishing. This requirement requires the polymer to possess a high enough molecular mass and a high conversion rate must be achieved. A high conversion rate also improves the radiation safety of the experimental setup, since less of the radiolabelled tracer remains in a volatile form. Polymerisation must also be accomplished in a bulk polymerisation setup, because solvents or emulsions could facilitate leaching from the sample matrix and present a radioactive

hazard. In addition, the polymerisation setup precludes the use of traditional polymer purification methods, rendering a pure product with a high conversion necessary.

The polymerisation mixture should be kept as simple as possible to minimise any potential sources of interference and reactions with sample matrix and other potential components in the impregnation mixture. Monomers bought from suppliers usually contain a small amount of an inhibitor compound, such as 4-methoxyphenol, to lengthen their shelf life. Because impregnations can last from several days to several months, it is prudent to leave the inhibitor in the mixture to reduce the chances of premature polymerisation and overpowering the inhibiting effect with a suitable amount of the initiator compound during the polymerisation phase. Other components in the impregnation mixture can include fluorescent dyes for double labelling. In addition, other components might have previously intruded into the sample matrix and the polymer fixes this component in place.

High conversion rates in bulk polymerisation carry the risk of overheating the mixture, because the mixture becomes increasingly viscous. This leads to bubble formation in polymer and sample breakage in extreme cases. When the gel effect sets in, the reaction rate increases quickly as the termination rate slows down (Odian, 2004). This results in a notable temperature increase. The amount of temperature increase may vary given reaction conditions and the initiation method (De Witte et al., 1977; Odian, 2004). Therefore, the reaction conditions must be set such that the reaction temperature does not increase beyond the boiling point of the monomer even when the gel effect sets in to avoid excessive bubbling. A lower radical concentration and, therefore, slower reaction rate can mitigate the gel effect. Yet, the reaction should proceed within a reasonable timeframe.

If the initiator is mixed into the impregnation mixture, it must be stable over a timeframe of possibly several weeks since the impregnant needs to intrude into the entire pore space of the sample before fixation by polymerisation. Most thermal initiators satisfy this requirement, but exclude the more reactive redox initiators that facilitate initiation at moderate temperatures (Odian, 2004). If, however, the sample is highly permeable and the redox system less reactive, adequate intrusion can be achieved for purposes such as conservation (Kotlík et al., 1980). The initiator compound must also be used in a suitable amount to overpower the inhibitor in the stock monomer mixture and carry out polymerisation to a good yield.

If irradiation is used as the initiation method, then a sufficient penetrative power is required to reach the monomer across all confines of the sample matrix. This requirement excludes non-ionising radiation and ionising radiation other than X-rays and gamma rays (Woods & Pikaev, 1994).

Due to these requirements, using ionising radiation has served as the preferred initiation method within the C-14-PMMA impregnation technique, although these requirements may be fulfilled using thermally decomposing initiators.

Ionising radiation can be used to initiate polymerisation (Odian, 2004). As such, electrons, neutrons, alfa particles, gamma rays and X-rays can be used. The exact reaction mechanism differs for each radiation type, but they all result in the formation of radical species. The formation of radicals commonly proceeds with the excitation caused by the radiation with the subsequent ejection of an electron:

$$A + radiation \rightarrow A^{+}\cdot + e^{-} \quad \{8\}$$

This kind of radical cation can dissociate to yield radical and cation species:

$$A^{+}\cdot \rightarrow B\cdot + C^{+} \quad \{9\}$$

The ejected electron may again associate with the cationic species:

$$C^{+} + e^{-} \rightarrow C\cdot \quad \{10\}$$

In addition, radicals can be produced through the following reaction sequence:

$$A + e^{-} \rightarrow A^{-} \quad \{11a\}$$

$$A^{-} \rightarrow B\cdot + C^{-} \quad \{11b\}$$

$$C^{-} \rightarrow C\cdot + e^{-} \quad \{11c\}$$

This radiolysis can result in cation, anion or free radical species, and all can initiate polymerisation. The monomer and reaction conditions dictate which of these species is the most prevalent. Radical species tend to predominate at higher temperatures, where ionic species are unstable. Aside from these reactions, radiolysis reactions leading to gas formation can occur (Siitari-Kauppi, 2002). Other common reactions consist of crosslinking, chain scission and peroxide formation in the presence of oxygen, which can lead to post-irradiation reactions

(Gould, 1967). Irradiation can also be used to graft monomers into already existing synthetic polymer chains (Gould, 1967) as well as biopolymers (Casimiro, et al., 2005).

Electron beam (EB) technology is commonly used for irradiation polymerisation since its penetration depth reaches much higher than that of ultraviolet (UV) and visible light (Odian, 2004). EBs, however, strongly attenuate in heavy materials, making these unsuitable for polymerisation deep within samples such as in rocks. In such cases, deeper-penetrating gamma radiation is more suitable. If, however, the polymer is just a film that needs to be cured, EB can be used to great effect (Langhals & Oginski, 2008). Due to the attenuation, gamma irradiation is required in the polymerisation of monomers impregnated within heavy samples. Gamma irradiation has also been successfully used in polymerisation within clay structures (Blumstein, 1965).

Gamma irradiation with a Co-60 source represents the basic method used in this technique (Hellmuth et al., 1994; Siitari-Kauppi, 2002; Sammaljärvi et al., 2012). The dose required for polymerisation is usually 50 to 80 kGy (Siitari-Kauppi, 2002), although for clay stone samples 100 kGy is necessary (Blumstein, 1965). At lower doses, the product often remained viscous (Siitari-Kauppi, 2002). This approach, however, requires an irradiation facility, which might not be readily available. In addition, this necessitates transporting the sample to an irradiation facility. The irradiation source also weakens over time due to the radioactive decay and replacing stock is expensive and not always simple. Furthermore, irradiation causes luminescence in quartz and feldspar minerals, which necessitates heat treatment before AG. Thus, this study investigated the application of thermally decomposing initiators—the mainstay of free radical polymerisation in general—for use within the C-14-PMMA impregnation technique.

Table 1 summarises the different aspects of the polymerisation of an impregnant in the pore system. During impregnation itself, the mixture must intrude well into the sample and not polymerise prematurely. The polymerisation reaction should proceed to a high conversion and be well-controlled to maintain a uniform distribution achieved during impregnation and to easily achieve a workable polymer–sample composite. The polymer produced should be rigid and, to withstand subsequent sample handling, present uniformly throughout the pore network in order to yield comparable results. All of this must be accomplished in a safe manner since the monomer itself is a volatile irritant with a radioactive label.

Table 1. Qualities of the desired polymer and ways of obtaining them

Desired quality	Attribute behind the quality	Solution
Rigidity	High molar mass, chain entanglement	Free radical polymerisation, bulk polymerisation
Uniformity throughout the sample	Initiation present throughout the sample	Gamma radiation, thermal initiation
Radiation safety	High conversion, low beta energy	Long reaction time, drying in fume cupboard
Good temperature control	Suitable radical concentration throughout the reaction	Suitable initiator concentration
Mixture stability	Lack of autopolymerisation, non-reactivity	Residual inhibitors not removed, storage in cool temperature, solutions kept suitably dilute, no protonating groups or good leaving groups
Wettability	Low contact angle and viscosity	Molecule with dipole moment near that of water

3.2. C-14-PMMA autoradiography and porosity calculation

C-14-PMMA AG images the spatial distribution of the C-14-labelled PMMA within the pore network of the sample along two dimensions. Film AG represents the most common method (Hellmuth & Siitari-Kauppi, 1990; Hellmuth et al., 1993; Hellmuth et al., 1994; Sammartino et al., 2002; 2003; Siitari-Kauppi 2002; Prêt et al., 2004; Kelokaski et al., 2006; Sardini et al., 2006; Leskinen et al., 2007; Siitari-Kauppi et al., 2007; Voutilainen et al., 2008; Voutilainen et al., 2012; Robinet et al., 2015). In film AG, the beta radiation from the tracer interacts with the silver halide in the film, producing a latent image. This latent image is then developed. The blackening of the film is proportional to the local activity. When the film is digitised, for example, using a table-top scanner, areas of different amounts of blackening are transformed into corresponding intensity values. Local optical densities are calculated from these intensity values and optical densities are converted to activities using a standard series. The local porosity can then be calculated using the activities known from the initial activity of the C-14-MMA tracer.

The intensities are converted into corresponding optical densities using the Beer–Lambert Law (Hellmuth et al., 1993; Hellmuth et al., 1994; Sardini et al., 2006). The Beer–Lambert Law

states that absorbance of a material is directly proportional to its thickness and the concentration of the absorbing species (Vogel, 1985) as shown in equation {12}:

$$OD_i = -log\left(\frac{I}{I_0}\right), \quad \{12\}$$

where OD_i is the local optical density, I is the intensity and I_0 is the background intensity.

Equation {12} is valid for integers in the range 1 to 256 for 8-bit images, with a value of 1 representing a perfectly blackened pixel and a value of 256 representing a completely non-blackened pixel, whereby the equation will produce optical density values between 0 and about 2.41.

Thus, the intensity is converted to optical densities by taking into account the background intensity. Optical densities can be converted into activities with the help of a calibration series composed of known activities. The relationship between the optical density of the film and the activity can be expressed using equation {13} as follows:

$$A_i = -\frac{1}{k} * ln\left(1 - \frac{OD_i - OD_0}{OD_{max}}\right), \quad \{13\}$$

where A_i is local activity [Bq], k is fitting coefficient [Bq^{-1}], OD_i is the local optical density, D_0 is the minimum optical density, OD_{max} is the optical density at the film saturation and OD_0, OD_{max} and k are calculated for each exposure using a series of C-14-PMMA standards.

Equation {13} is an experimentally derived equation, which is valid when the value of OD_i is between OD_0 and OD_{max}. Local activity value A_i can only be equal to or below A_o, which represents the activity of the pure tracer.

Using these two equations, the local activity can be solved and placed into equation of porosity {14}. The beta correction must be taken into account in the porosity calculation due to the range of C-14 beta emissions in materials of different densities. Thus, the beta correction is proportional to the sample's grain density and the PMMA density (Hellmuth et al., 1993; Hellmuth et al., 1994; Sammartino et al., 2003; Kelokaski et al., 2006). Here, a grain density of 2.7 g/cm^3 for rock material and a PMMA density of 1.2 g/cm^3 are used:

$$\phi_i = \frac{\frac{\rho_m}{\rho_{resin}}}{1 + \frac{A_i}{A_0} * \left(\frac{\rho_m}{\rho_{resin}} - 1\right)} * \frac{A_i}{A_0}, \quad \{14\}$$

where φ_i is the local porosity [%], ρ_m is the material grain density [g/cm^3], ρ_{resin} represents the PMMA resin density [g/cm^3], A_i is local activity [Bq] and A_0 is tracer activity [Bq].

The equation {14} produces values between 0 and 1. A value of 0 corresponds to zero porosity, while 1 corresponds to open-hole full pure PMMA. The calculation as shown in equation {14} is completed for all pixels in the selected area of the image and results are provided as histograms or profiles.

A proprietary program based on the Matlab Image Analysing Toolbox was used to calculate the calibration parameters and quantitative porosity values. Figure 4 shows a typical calibration curve AG standard. In addition, porosity maps can be created by matching the porosity values calculated from grey-scale AGs to colours for better contrast. This approach can yield a clearer image on the local differences in porosity, although grey-scale AGs sometimes show discrete features more clearly.

In storage phosphor screen–based AG, the imaging process is different. The beta radiation interacts with the europium-bromine-phosphor complex in the imaging plate, causing the complex to transition to a higher excitation state. This excitation can then be relaxed using laser light. This relaxation produces a blue light of a specific wavelength and is then collected by a scanner specifically designed for such a purpose, for example, Fuji FLA-5100. The amount of blue light produced from any given location depends on the local activity. The scanner collects the light pulses from the sample and leads them to the amplification tube and, from there, to an analogue–digital converter, which then inputs the digitised values into a computer. This produces a 16-bit digital image.

For phosphor screen AG, the optical densities are calculated according to equation {15} (Sardini, et al., 2015) as follows:

$$OD = OD'_0 * A^{k'}, \quad \{15\}$$

where OD is the optical density, OD'_0 is the optical density for A = 1 Bq/ml, A is the local activity and k' is the fitting coefficient.

This equation can be converted to equation of local activity {16}

$$A = \left(\frac{OD}{OD'_0}\right)^{\frac{1}{k'}}. \quad \{16\}$$

The local activity values given by this equation can then be inputted into equation {14}. Porosities are then calculated from the optical densities or by converting directly from the grey values to activities using a standard series.

In terms of quantitative AG, a 16-bit image using phosphor screen AG has the advantage of a wider linear range. This translates into smaller uncertainties since the error tends to increase towards very low and very high grey values for film AG.

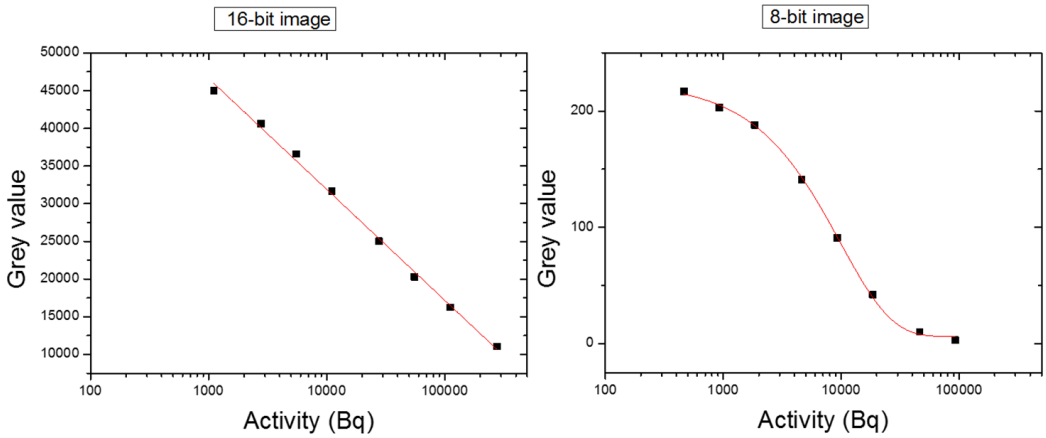

Figure 4. Typical calibration curves for digital autoradiography (left) and film autoradiography (right)

Compared to other porosity measurement methods, some differences may arise in the results. For instance, compared to water gravimetry, slightly lower porosities are often obtained particularly in rocks with porosities of less than 1%. This may result due to an incomplete intrusion, a threshold energy for AG not exceeding those in areas of low activity and the use of the non-linear region of the calibration curve (Siitari-Kauppi, 2002). Among these problems, incomplete intrusion can be mitigated by lengthening the impregnation times and ensuring the complete removal of residual water in the sample matrix. Not exceeding the threshold energy can be mitigated by a longer exposure time. The use of a non-linear range on the calibration curve is less problematic when the storage phosphor screen imaging plates are used, since they have a wider linear range than X-ray films. Compared to mercury porosimetry, the best agreement lies in a porosity range greater than 1% (Siitari-Kauppi, 2002). Overall,

given the different strengths and weaknesses of various measurement techniques, using several methods in any given experiment proves useful.

3.3. C-14-PMMA impregnation technique applications

Many applications of the C-14-PMMA impregnation technique primarily focus on crystalline rock, although sedimentary rocks have also been studied. In addition, man-made materials such as cements have been studied using the C-14-PMMA impregnation technique. More recently, studies have focused on the interface between natural and man-made materials.

During initial investigations, the spatial distribution of porosity was studied in Lavia granodiorite and Olkiluoto tonalite (Hellmuth et al., 1993), subsequently examining rapakivi granite, muscovite granite, sedimentary iron ore (Hellmuth et al., 1994) and weathered marble (Hellmuth et al., 1999). The C-14-PMMA impregnation technique has also been adapted to studying geological barriers in spent nuclear fuel deposition (Siitari-Kauppi, 2002; Kuva et al., 2012). Soon after its initial development, the C-14-PMMA impregnation technique was combined with other characterisation techniques to obtain supporting or complementary information. C-14-PMMA AG and He-gas pycnometry have been applied to investigate changes in the porosity, permeability and diffusivity of an excavation-disturbed zone at the Olkiluoto repository site (Autio, et al., 1998). A somewhat similar study was undertaken to characterise granite from a quarry in France. In that study, porosity changes were examined using C-14-PMMA AG combined with mineral surface staining and electron microscopy (Robert, et al., 2003). The pore-space geometry of Grimsel granodiorite has been examined through complementary analyses using polarisation microscopy and mercury porosimetry (Kelokaski et al., 2006). Furthermore, a combination of X-ray tomography, confocal laser spectroscopy and C-14-PMMA AG was used to study different granites (Lähdemäki, et al., 2007). Mineral staining to obtain mineral-porosity correlation with supporting parameters analysed via water gravimetry, electron microscopy and He-gas pycnometry have been completed (Sardini et al., 2006). Grimsel, El Berrocal and Los Ratones granite mineral-specific porosities have been investigated in conjunction with field emission SEM (FESEM)/EDS (Leskinen et al., 2007). Sievi granite structural and mineralogical heterogeneities were investigated through C-14-PMMA AG, X-ray microtomography and FESEM-EDS analyses. These results were then used to construct a 3D model of the sample (Voutilainen, et al., 2009).

X-ray tomography analysis together with C-14-PMMA AG were also performed on altered tonalite (Voutilainen, et al., 2012). Likewise, C-14-PMMA AG and X-ray tomography were used to study the weathering processes of Bishop Creek granite (Mazurier, et al., 2016).

Sedimentary clay rocks have also been studied. The spatial distribution of calcareous shale and the problem of handling highly porous areas were investigated (Sammartino, et al., 2002). In addition, the spatial distribution of the porosity and mineral in clay rock from the Callovo–Oxfordian formation were studied to understand the possible implications for the diffusion of ionic species and the rock sorption capability (Sammartino, et al., 2003). The same formation has also been subject to a porosity upscaling study, wherein H-3-PMMA AG was combined with electron microscopy (Robinet, et al., 2015). Similarly, the porosity distribution in a clay gouge from the St. Julien Basin was studied using C-14-PMMA AG and FESEM imaging (Prêt, et al., 2004). Likewise, sandstone from the Athabasca Basin was examined using C-14-PMMA AG and electron microscopy (Sardini, et al., 2009). Finally, clay samples from the Boda, Boom and Opalinus formations were compared using C-14-PMMA AG and electron microscopy supported through analyses based on X-ray diffractometry and mercury porosimetry (Parneix, et al., 2012).

Furthermore, man-made materials have also been studied through C-14-PMMA AG. Modelling of the induced chemo-mechanical stress of cement mortar affected by CO2 was studied through the application of C-14-PMMA AG (Jeong, et al., 2013). Shrinkage and porosity changes caused by CO2 carbonation were modelled using the micro-dilatation theory and the calculated results were verified experimentally using C-14-PMMA AG (Jeong, et al., 2015). In addition, porosity changes in the interface between Portland cement paste and argillite claystone were studied using C-14-PMMA AG, with additional analyses based on electron microscopy, X-ray diffractometry, thermogravimetric analysis and X-ray microtomography (Lalan, et al., 2016). The porosity changes over a 15-year period in a cement–argillite interaction have also been studied using C-14-PMMA AG (Gaboreau et al., 2011). A similar approach has been undertaken to study the porosity changes in a five-year interaction experiment of Opalinus clay and cement (Mäder et al., 2017).

Overall, the two most common techniques coupled with C-14-PMMA AG consist of X-ray microtomography and SEM imaging. This is the case because X-ray microtomography allows for the complementary measurement of porosity. Furthermore, it is possible to obtain 3D

information on various mineral phases of a sample, and SEM imaging and the associated EDS measurements provide a direct examining of the local sample morphology and mineralogy.

3.4. Development needs addressed in this work

Based on a review of the literature and empirical evidence, we identified several development needs for the C-14-PMMA impregnation technique. These needs concern the initiation of the polymerisation reaction, intrusion of the impregnant into moisture-sensitive materials and support for other characterisation techniques.

3.4.1. Initiation system development

Thermal initiators produce radicals by decomposing above certain compound-specific temperatures (Odian, 2004). Such an initiator must dissociate at a fast enough rate to achieve polymerisation in a reasonable time, but not too quickly. A pure thermal initiation is possible for some monomers, but is typically too slow to deliver reasonable conversion rates within a reasonable timeframe. The radical production proceeds via general reaction {17}:

$$I \xrightarrow{\Delta} R\cdot \qquad \{17\}$$

where Δ symbolises heat.

This dissociation reaction typically produces two similar radical species, but can also produce two different radical species or even a radical and a non-radical species (Odian, 2004). Thermal initiators such as benzoyl peroxide (BPO) and azobisisobutyronitrile (AIBN) can be used to initiate radical polymerisation. The radical production reactions for BPO and AIBN are illustrated in {18} and {19}:

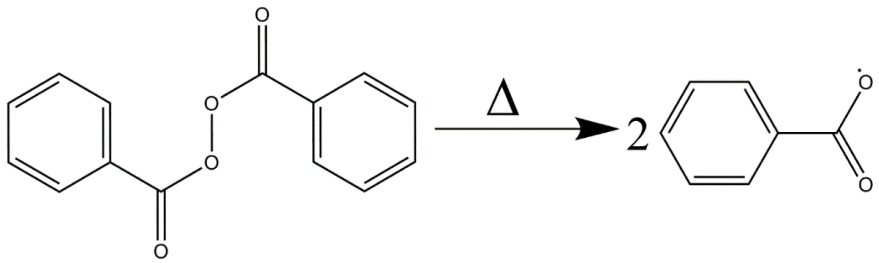

{18}

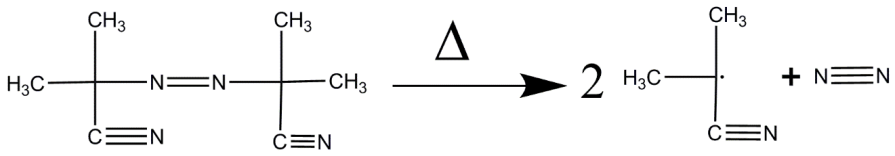

[19}

Compared to the reaction schema for irradiation-initiated polymerisation reactions {8–11c}, the radical production reaction scheme of thermally initiated polymerisation as shown in general reaction {17} and in detail in reactions {18–19} are slightly simpler. The monomer radiolysis reactions and other radiation-induced reactions are also absent, although other side reactions can of course occur depending on the reaction system. A crucial similarity, however, exists since the time-initiator concentration equation of thermally initiated polymerisation appears analogous to the time-dose rate equation of irradiation polymerisation. Therefore, comparable polymers can be produced following suitable adjustment to the initiator concentration and reaction temperature (Beall & Witt, 1972).

This type of polymerisation can be easily performed in a laboratory setting. Furthermore, these reactions produce reactive radical species within reasonable timeframes allowing polymerisation to a high conversion within a few hours to a few days depending on the reaction setup. In addition, such reactions are also adequately stable at room temperature, although cooled solution storage diminishes the chance of premature polymerisation or autopolymerisation.

The initiator concentration and the heating programme can be tailored, within certain limits, to suit the specific needs of a given reaction system. The lower limit for the initiator concentration lies where the radical production can overcome the residual inhibitor in the monomer solution to reliably produce a high conversion rate polymerisation. While the inhibitor can be removed from the mixture, the removal may increase the chance of premature polymerisation. The C-14 label itself is a beta emitter, which can also act as an

initiator. Therefore, it is better to simply add an excess of the initiator that can overcome the inhibition. Alternatively, it is best to keep it as low as possible, while maintaining near-total conversion rates. A higher initiator concentration increases the risk of overheating and premature polymerisation during impregnation. Thus, a balance must be found between the reliability of the polymerisation and the risk of any adverse effects.

The initiation system development must also take into account that an initiator must be able to intrude into the same space as the impregnant monomer itself. It appears that only polar molecules can penetrate the interlayer space in clays (Blumstein, 1965). Polar initiator compounds are, however, available. For instance, BPO exhibits polar oxygen–carbon bonds and AIBN exhibits polar carbon–nitrogen bonds. Fully aliphatic initiators, however, would be unable to enter such small pore spaces. In addition, clay/polymer composites have also been successfully prepared with thermal initiators such as BPO and AIBN in both unmodified (Blumstein, 1965) and modified clays (Wang et al., 2002; Liu, et al., 2003; Zeng & Lee, 2001).

Furthermore, the initiator should be non-reactive towards the geomaterials. BPO was found to decompose in the presence of iron (II) (Hasegawa & Nishimura, 1960). Yet, the iron (II) concentration used in Hasegawa and Nishimura's experiments were quite high and precautions were taken against inhibition processes. In the case of the C-14-PMMA impregnation of geomaterials, the expected concentration of free iron (II) should be significantly lower and the residual inhibitor typically remains in the monomer mixture. Therefore, premature redox reactions of primarily thermal initiators such as BPO are not likely a major problem, except perhaps in the case of stones containing large amounts of wüstite or magnetite or in the presence of iron (II)-rich pore waters. In such cases, other thermal initiators could be used.

3.4.2. Water-soluble monomers for moisture-sensitive applications

HEMA, as shown in Figure 5, is a water-soluble monomer (Montheard et al., 1992), with a hydroxyl functional group in its pendant group. It can be mixed with MMA, whereby the resultant mixture is then sufficiently water soluble to penetrate into water-filled spaces. Despite its higher viscosity, HEMA appears capable of entering into the interlayer space of clays where it can undergo polymerisation using thermal initiators (Koç et al., 2013) and

photoinitiators (Fecchio et al., 2016). Its suitability for impregnation of highly porous materials such as bricks, gypsum and sedimentary rocks has also been investigated (Hellmuth et al., 2011). The hydrophilicity can be useful in an in situ experiment wherein complete drying of the sample material is laborious and difficult to achieve. A polymer made entirely of HEMA is quite soft and the monomer itself is more viscous than water or MMA (Hellmuth et al., 2011). Yet, when mixed with MMA in a sufficient ratio, the impregnation can be rapid, while still maintaining the hydrophilic character and the resulting copolymer will be sufficiently rigid for C-14-PMMA AG. The activity of the copolymer is still contained in the C-14-MMA and dilution by the comonomer must be taken into account in the calculations. Because HEMA has a higher viscosity than MMA, longer impregnation times may be necessary.

HEMA-based copolymers have been previously used to form a consolidating film on terracotta artefacts (Langhals & Oginski, 2008), noting that the copolymer can be used for wet materials as well.

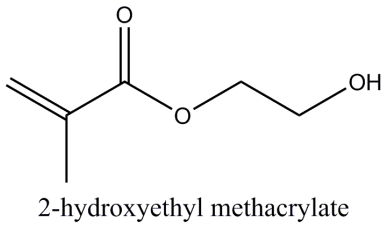

Figure 5. Chemical structure of 2-hydroxyethyl methacrylate (HEMA)

3.4.3. Support for other imaging techniques

The limits of possible achievements through the combination of the C-14-PMMA impregnation technique with others continues to be stretched. C-14-PMMA impregnation technique development has broadened the possible range of applications, and technological developments, including storage phosphor screen AG, allow for better measurements and we seek to continue this wholesome development. In geomaterials studies, we also seek to improve upon previous achievements by applying different measurement techniques in tandem. Pore aperture measurement can be challenging if measured purely from autoradiographs due to the resolution limits of the beta radiation range, although progress has been made on the aperture estimation using AG in combination with simulation (Sardini

et al., 2014). SEM imaging is, however, well-suited towards this task (Sprunt & Brace, 1974). The pore apertures obtained via SEM can then be combined with spatial information to link them to specific areas in autoradiographs. Through EDS measurements, it is also possible to measure the composition of the possible pore fillings. The composition of fracture fillings has been measured in granitic rock (Sahlstedt et al., 2014). Yet, this has not been carried out on a micro-pore scale at Olkiluoto.

In addition, we identified as a development point the possibility of using contrast agents for improved imaging in the two imaging techniques most commonly combined with the C-14-PMMA impregnation technique—that is, X-ray tomography and SEM–EDS. C-14-PMMA does not bring any notable additional contrast to X-ray tomography or SEM compared to the mineral phases due to the low average Z-number of the compound. Fluorescent dyes have been dissolved in MMA to improve the contrast in optical microscopy (Lähdemäki et al., 2007; Hellmuth et al., 2011). Furthermore, the complexation of metal ions such as Co(II), Cu(II), Pb, Eu(III) and U complexed using thenoyltrifluoroacetone has been examined (Hellmuth et al., 2011). These complexes are quite soluble in MMA, and the Cu and U complexes were identified in rock pores using SEM, although the signal strength was an issue and a long measurement time was necessary. While contrast agents such as Wood's metal have also been used in the characterisation of geomaterials using SEM, intrusion appears to be a pressure-driven process. Yet, this pressure can create artefacts (Klaver et al., 2015). Furthermore, in some cases, the spatial distribution porosity information resulting from C-14-PMMA AG is not necessary or cannot be properly exploited. Handling samples containing radioactive materials might also be cumbersome or unwelcome.

Therefore, we aimed to test a contrast agent to mix with the tracer to improve the contrast in both SEM and X-ray tomography, which does not require artefact-creating pressurisation and could be fixed in place via the C-14-PMMA impregnation technique. Based on the literature review, it appeared that filling the pore space with an artificial precipitate tends to hinder flow and permeability rather than completely blocking it (Chagneau et al., 2015; Noiriel et al., 2016), suggesting that such a two-part impregnation can be accomplished.

4. Experimental

4.1. Materials

The materials used in these experiments primarily consisted of geomaterials, with man-made brick as a test material. We used brick in article I as the test material. Brick, a ceramic material with several favourable properties regarding its use as a test material, possesses a high porosity and conductivity and was pre-treated at high temperatures.

Grimsel granodiorite, used in articles I and IV, consisted of samples collected from the Grimsel Test Site (Switzerland). Its mineral composition includes K-feldspar, plagioclase, quartz, biotite and small amounts of muscovite, apatite, sphene, epidote, zircon, chlorite, calcite and ore minerals (Kelokaski et al., 2006). As a well-studied material (Möri et al., 2003) with a fairly conductive pore system, Grimsel granodiorite allows for impregnation times on a reasonable time scale.

Olkiluoto pegmatitic granite and veined gneiss were used in article III. Pegmatitic granite exists as veins and irregular bodies in the bedrock of Olkiluoto area, and is primarily composed of quartz, plagioclase, K-feldspar, muscovite and other accessory minerals.

Olkiluoto veined gneiss is one of the main rock types in the Olkiluoto bedrock. This rock type was studied in articles III and IV, and is composed primarily of biote, quartz, K-feldspar, plagioclase, cordierite, sillimanite, muscovite and small amounts of other minerals. Due to the strong heterogeneity in the leucosome veins of this rock type, one sample can have a markedly different composition compared with another (Ikonen et al., 2015).

Opalinus clay samples, originating from the Mont Terri site (Switzerland), were used in article II. The Opalinus clay formation is a 80- to 120-m-thick subhorizontal formation in northern Switzerland, consisting of well-consolidated, grey-to-black micaceous marine shale with calcareous horizons. There are also beds and lenses of sandstones and siltstones. Mineralogically, Opalinus clay primarily consists of phyllosilicates framework silicates, carbonates and quartz. Several facies of differing compositions have been identified in the formation. Shaly facies typically contain 20% quartz, 7% calcite and 65% clay minerals. Sandy facies typically contain 30% quartz, 15% carbonates and 40% clay minerals. Carbonate-rich sandy facies typically contain 30% quartz, 40% calcite and 20% clay minerals (Pearson et al., 2003). The samples studied in article II came from this facies.

4.2. Reagents

Reagent-grade methyl methacrylate was used in all of the experiments. Both inactive and C-14-labelled varieties were used. The inactive MMA (Merck) was of a synthetic grade and had a purity in excess of 99%. The C-14-MMA solutions were dilutions of the labelled monomer from the Pharmaron UK ltd (Cardiff, United Kingdom).

Reagent-grade HEMA (Aldrich) was used in article II, with a purity of 97% and stabilised using 200 ppm of hydroquinone. All HEMA used in the experiments were inactive and, therefore, all of the activity measured comes from the C-14-labelled comonomer MMA.

Benzoyl peroxide (BPO) (Merck) was used in all of the experiments, with a purity of 75%, the remainder of which consisted of water. It was used without further purification.

Kodak BioMax MR films were used for AG in articles I through III. This type of film is optimised for the detection of isotopes such as ^{14}C. The films were developed in a darkroom under a red light, using Kodak processing chemicals for the AG film developer from Sigma-Aldrich (PT7042) for development and Kodak GBX fixer (Cat 190 1875) for fixation. These films were then scanned using a Canon 9900F table-top scanner.

Fuji BAS TR2025 imaging plates were used in article III to provide supporting AG measurements, scanned using a Fuji FLA5100 scanner.

4.3. Experimental plan

The polymerisation methods for thermally initiated polymerisation were developed. For different monomer mixtures, different heating methods might be necessary. We tested the developed methods in typical sample matrices and the obtained data were combined with other techniques.

Articles I and II focused on method development. In article I, different initiator concentrations and heating programmes were tested for the thermally initiated polymerisation of MMA. These tests were followed by analyses on different sample matrices to determine if any interference arose from the sample matrix. The tested matrices consisted of brick and Grimsel granodiorite. Brick was selected because it was an easily available material that has a high permeability and porosity. This translates into short intrusion times and a porosity that can be

readily quantified using a variety of techniques. Grimsel granodiorite was chosen because it was a good representative of the rock type commonly investigated using this technique.

The conversion rates under the different reaction conditions were measured by following the ratio of the monomer double-bond signal to the signals originating from the polymer backbone using ^{1}H-NMR. The molar masses of the polymers produced under these different reaction conditions were measured using gel permeation chromatography (GPC). Both of these measurements were calculated using crushed samples of brick and Grimsel granodiorite or pure polymer in the case of vial polymerisations.

Preliminary analyses of the bulk porosities of brick and Grimsel granodiorite were carried out using water gravimetry. The porosities of the impregnated samples were subsequently measured using thermogravimetric analysis and C-14-PMMA AG. We compared the porosity results over the different measurement techniques to each other and to values found in the literature.

Figure 6 illustrates the optimisation process of the thermal polymerisation of MMA in different matrices.

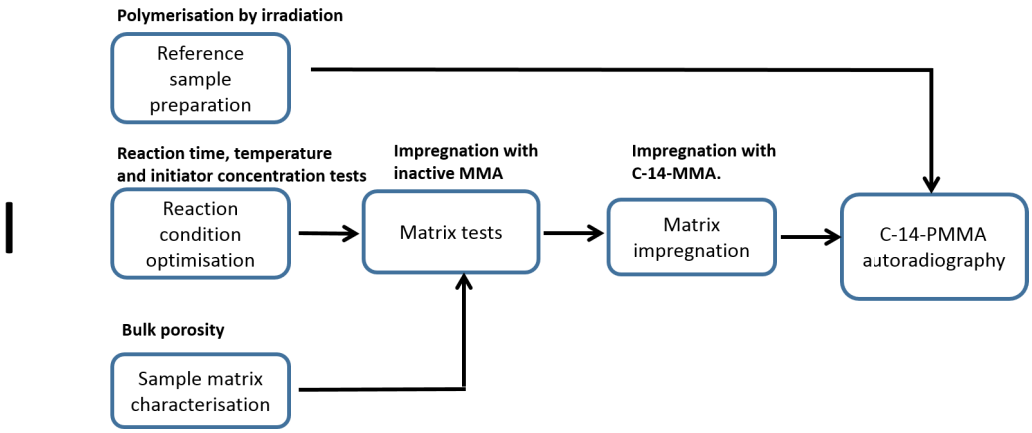

Figure 6. Development process for the thermally initiated polymerisation of MMA in brick and Grimsel granodiorite from article I

Suitable sample matrices were then impregnated with an HEMA/MMA solution and polymerised, and then compared to sample matrices impregnated with just MMA as the sole monomer. The use of the hydrophilic monomer HEMA was tested in Opalinus clay. Opalinus clay is a good representative of mostly non-expanding clay. Another goal of this work focused on ascertaining how potential coring damage could be seen in the autoradiographs (article II). FESEM imaging was performed on the thermally polymerised samples to ascertain what changes are associated with coring damage. The semiquantitative mineral composition of the Opalinus clay was determined using X-ray diffraction.

Mixtures of HEMA and MMA were also tested on clay samples (article II). As such, we tested different initiator concentrations, monomer feed ratios and heating programmes. The testing regimen was broadly similar to the optimisation process for the thermally initiated polymerisation of pure MMA. Figure 7 illustrates this process.

Porosities were measured for three types of samples: Opalinus clay impregnated with 100% C-14-MMA and polymerised with gamma irradiation; Opalinus clay impregnated with C-14-MMA and polymerised with the aid of a thermal initiator; and Opalinus clay impregnated with a mixture of 75% HEMA and 25% C-14-MMA and polymerised with a thermal initiator. The porosity values were obtained using C-14-PMMA AG, thermogravimetry and a comparison to values found in the literature.

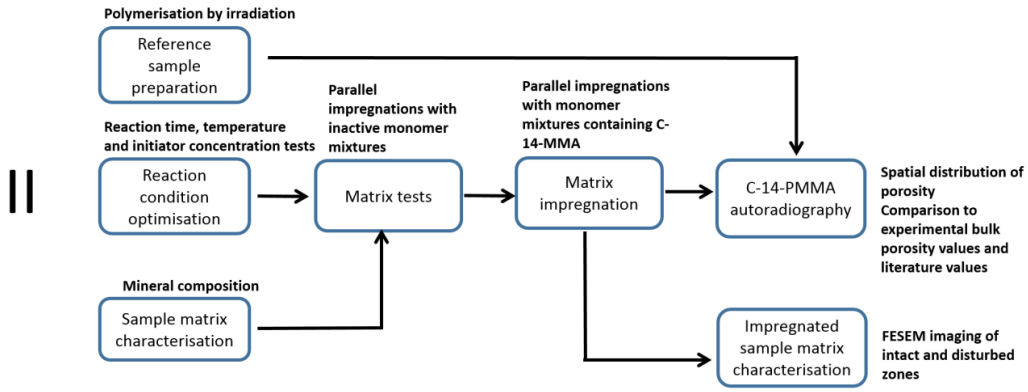

Figure 7. Development process for the thermally initiated polymerisation of two different methacrylate mixtures in clay rock from article II

Articles III and IV focused on application development. More specifically, article III focused on combining pore aperture and pore filling data from SEM and spatial porosity data from C-14-PMMA AG. The rock types studied using this approach consisted of pegmatitic granite and veined gneiss from Olkiluoto used in in situ diffusion experiments at the Olkiluoto repository site (Voutilainen et al., 2014). The bulk porosities and overall mineral compositions were previously investigated (Ikonen et al., 2015). These rock samples were impregnated with C-14-MMA and polymerised using the methods developed in this work. The polymerised samples were then sawed and polished and the same sample surfaces were used for both C-14-PMMA AG and SEM analyses. Figure 8 illustrates this process.

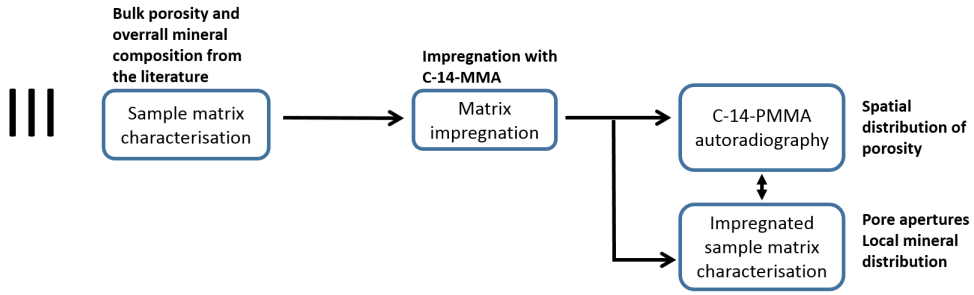

Figure 8. Characterisation process of the mineral porosity of pegmatitic granite and Olkiluoto veined gneiss in article III

Article IV focused on the development of the contrast agent for imaging the connected porosity via X-ray tomography and SEM. Caesium chloride (CsCl) was chosen as the contrast agent and was intruded into Olkiluoto veined gneiss and Grimsel granodiorite sample matrices. We tested different immersion times to ensure full intrusion of the contrast agent. The samples were imaged with X-ray tomography before contrast agent fixation. This was followed by impregnation with MMA and polymerisation into PMMA. Thus, this contrast agent addition involves two distinct steps and the pores already have fillings when the MMA intrudes into them. The contrast agent–laden samples were then imaged again using X-ray tomography and additionally using SEM. Figure 9 illustrates this process.

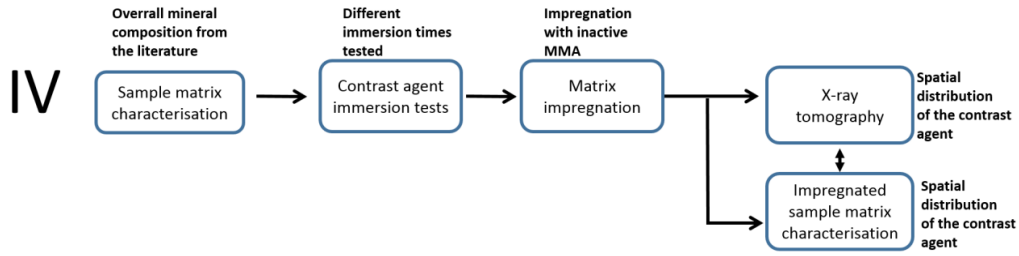

Figure 9. Development process for imaging connected porosity in crystalline rock using the contrast agent–aided X-ray tomography and electron microscopy from article IV

5. Supporting characterisation techniques

5.1. Porosity characterisation

5.1.1. Water gravimetry

Water gravimetry is based on measuring the amount of water soaked by the sample or, conversely, drying a saturated sample to a constant weight (Melnyk & Skeet 1986). Using this method (International Society for Rock Mechanics, 1979), the samples are first dried to a stable weight. The sample is then immersed in water and the weight is measured at set intervals. Once the weight no longer changes after several measurements, all of the connected porosity has been filled with water. This saturated weight is then compared to the dry weight of the samples. The ratio represents the connected porosity of the sample as measured by water gravimetry. Water gravimetry measurements should always be completed in exactly the same manner, preferably by the same person, since minute changes in the measurement method can alter the results. Despite this, there is still a notable amount of uncertainty in the final result. Water gravimetry also only provides the connected bulk porosity yielding little information about the pore structure. Some conclusions regarding the overall pore structure can be deduced from the saturation curve. For instance, the shape of the saturation curve can provide the ratio between quickly filled highly connected porosity and more slowly filled porosity.

Water gravimetry was used in article I. Here, the samples were first dried to a constant weight in an oven at 105°C for at least 24 h. This was followed by saturation and weighing the samples until no increase in the wet mass was noted. Thereafter, the samples were dried to a constant mass. The samples were primarily 15-mm-thick rock cores with diameters of 38 to 45 mm.

5.1.2. Thermogravimetric analysis (TGA)

Thermogravimetric analysis (TGA) measures the change in mass resulting from a temperature change (Coats & Redfern, 1963). In porosity measurements, the tracer pyrolysed and released from the pores is measured. In addition, TGA has been used to ascertain the amount of PMMA external to the sample clay matrix as well as the amount within the clay matrix lamellae (Blumstein, 1965). TGA measures the connected bulk pore space wherein the tracer intruded (Möri, et al., 2003). Thus, the sample matrix ideally remains stable over the temperature

programme. If it does not, the matrix decomposition should also be measured. For instance, cement (Scrivener, et al., 2004) and clays (Mielenz et al., 1953) represent porous materials whose compositions affect the TGA curve.

In articles I and II, we used TGA. As such, TGA samples were prepared by crushing rock samples in a mill, collecting 40 to 90 mg of sample powder for a single analysis.

5.2. Imaging techniques

5.2.1. Scanning electron microscopy (SEM) with energy dispersive X-ray spectroscopy (EDS)

Scanning electron microscopy (SEM) relies on bombarding a sample with electrons, which are then deflected from the sample surface and from a short distance underneath or which detach secondary electrons (SE) from the sample structure (Friel, 2003). Secondary electrons provide information on the sample material morphology. Backscattered electrons (BSEs), by contrast, yield more information about the phases of differing sample densities. This can be used to separate different minerals in geomaterials (Lloyd, 1987). Electron microscopy can be combined with energy dispersive X-ray analysis (EDS) to ascertain quantitative elemental compositions. When an electron of sufficient energy strikes the atom, it can eject one of its own electrons from the inner shells. This causes another electron from the outer shells to replace the ejected electron, a process accompanied by the release of characteristic X-rays. In an energy dispersive spectrometer, the X-ray energies are absorbed by the detecting material producing pulses in the detector proportional to their energy (Friel, 2003). When studying geomaterials, EDS can be used for elemental mapping (Anovitz & Cole, 2015).

In articles II, III and IV, we relied on SEM imaging in SE and BSE mode and EDS, using a Hitachi S-4800 model with an Oxford Instruments Inca X-Sight X-ray diffractometer. Some analyses were also performed using a Jeol JSM-7100F Schottky with an Oxford Instruments EDS system.

5.2.2. X-ray tomography

X-ray tomography measures the differences in X-ray attenuation within a sample (Voutilainen, 2012; Kuva, 2016). Generally, this corresponds to the different densities of various phases in a specific material. In geologic materials, for example, different minerals have different

densities. The various areas with different attenuation coefficients appear as different shades of grey. The X-ray tomograph scans the sample producing a 2D image. The sample is then rotated in small increments with a scan taken at each step. Completing a scan over the entire depth of a sample can produce a reconstructed 3D-voxel map of the sample. Typically, the analysis of tomographic images requires considerable image analysis. This image analysis improves the quality and detectability of the details and allows for segmentation. The quality of the tomographic images can be improved both within the measurements by adjusting instrument settings and in the image reconstruction by adjusting the image handling parameters. Segmentation is used to differentiate the component phases of samples. Micrometre-scale tomography represents the most common scale for X-ray tomography in geomaterials, although nanometre-scale tomography is also possible. The choice of scale depends on the scale of the features examined.

We used X-ray tomography in article IV, performed using a SkyScan 1172 table-top scanner. Imaging was completed at a 6.1-µm voxel size using a source voltage of 100 kV and a source current of 80 uA. The images were reconstructed using the SkyScan NRecon software.

5.3. Polymer characterisation techniques

5.3.1. Nuclear magnetic resonance spectrometry (NMR)

Nuclear magnetic resonance (NMR) spectroscopy measures the effects of the local chemical environment on the magnetic properties of nuclei (William & Fleming, 1995). When placed in a magnetic field, the NMR active nuclei absorb at a frequency characteristic of the isotope. The local chemical environment causes slight changes to this frequency. Both this frequency and the fundamental resonance frequency are directly proportional to the magnetic field strength. Thus, the frequency shift can be converted into a field-independent dimensionless value called a chemical shift. The chemical shift is typically reported relative to a reference frequency. Because all nuclei emit unique signals depending on their chemical environment, information regarding the molecular structure can be obtained (Williams & Fleming, 1995). The size of the peaks is also proportional to their number in the molecule and in the overall sample. Therefore, the peak integrals can be used to measure the conversion (Odian, 2004).

We used NMR in article I and in the preliminary analyses performed in article II to determine the conversions of the tested polymerisation reactions. NMR samples were prepared using solid-phase extraction of the sample powder with a suitable solvent, typically $CDCl_3$. The amount of sample powder required depended on the porosity of the sample.

5.3.2. Gel permeation chromatography (GPC)

In gel permeation chromatography (GPC), the solution is run through a column filled with porous gel particles (Odian, 2004). The separation of the solutes relies on size of the hydrodynamic volume of the solutes. Smaller solutes experience an increased retention in these porous particles since they can enter them. Therefore, the solutes exit the column in decreasing order of hydrodynamic volume. This hydrodynamic volume is proportional to the molar mass of the solute and, with a standard set of a suitably similar chemical nature, the molar weight and the molar mass distribution can be measured.

We used GPC in article I to ascertain the molar masses of the polymers produced under reaction conditions. As noted in Table 1, rigid and well-entangled polymers are necessary, and this is achieved via high molar mass polymers. We also used GPC to attempt measurement of HEMA-based polymers in article II, but these could not be dissolved in any available GPC solvents. GPC samples of impregnated rock samples were prepared via solid-phase extraction of the sample powder using tetrahydrofuran. The required amount of sample powder depends on the porosity of the sample. Therefore, brick samples required only about 20 mg and crystalline rock samples required about 600 mg of sample powder.

6. Results and discussion

6.1. Thermally initiated polymerisation of MMA in brick and Grimsel granodiorite (article I)

The initial method development aimed to produce similar end results with thermally initiated polymerisation as those previously obtained via irradiation polymerisation. Towards this end, we tested different initiator concentrations, temperatures and reaction time conditions. The optimum conditions consisted of 0.5% (w/w) BPO and a 16-h heating programme at 55° C. These conditions were tested in brick and Grimsel granodiorite matrices, finding that no harmful interference occurred from the sample matrices.

Granitic rock is a typically fractured, low porous rock with grains ranging from a micrometre to centimetre scale. Because the pores of granitic rock are mostly of a micrometre scale, we expected that adding an initiator compound to the mixture would do little to hinder the intrusion of the tracer mixture. Herein, we compared results from thermally and radiation-initiated polymerisation. Supporting data were obtained for porosity via water gravimetry and thermogravimetry. We analysed the conversions and molar masses of the resulting polymers using ^{1}H-NMR and GPC, respectively. Conversions primarily reached in excess of 90%. At this level of conversion, the plasticising effect of a residual monomer is low enough that the polymer remains quite solid. It does, however, present some radioactive hazard, which can be counteracted by allowing the residual monomer to evaporate in a fume cupboard. The molar masses as determined using GPC were high enough to result in rigid polymers. The porosity results obtained were in good agreement across various methods. Table 2 provides a summary of these results.

Table 2. Average results for the thermally initiated polymerisations of MMA in different matrices. All reactions carried out at 55° C for 16 h. Results from article I.

	Sample type		
	Vial	**Brick**	**Grimsel granodiorite**
Conversion (%)	96.0	98.4	92.5
M_n (g/mol)	530 514	671 600	910 450
M_w (g/mol)	729 295	897 750	1 081 500
M_w/M_n	1.37	1.33	1.22
Porosity by TGA (%)	—	31.7±0.2	1.0±0.4
Porosity by autoradiography (%)		31.4±3.1	0.9±0.1
Porosity by water gravimetry (%)		32.0±0.1	0.8±0.1

We performed AG on samples impregnated and polymerised according to the developed procedures. Figure 10 provides examples of these autoradiographs. Here we can see that impregnation appears to have been complete and no polymer was leached during sample handling.

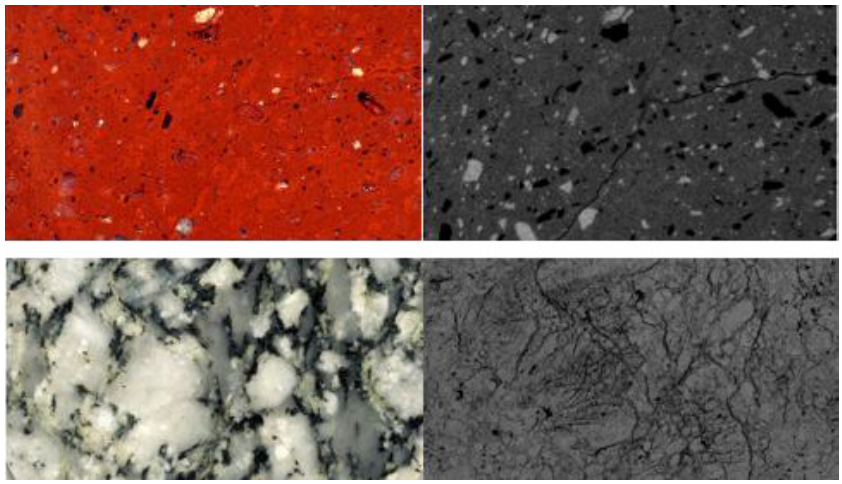

Figure 10. Surface scan (top left) and corresponding film autoradiograph (top right) of brick. Surface scan (bottom left) and the corresponding autoradiograph (bottom right) of Grimsel granodiorite. Sample is 3 cm in both cases. Figure adapted from article I.

Overall, thermally initiated polymerisation produced results similar to those obtained via irradiation-initiated polymerisation (Kelokaski et al., 2006; Sardini et al., 2006; Leskinen et al., 2007). Based on the success here, the next step aimed to test similar procedures on fine-grained clay rock. Therein, we could evaluate copolymerisation with water-soluble monomers such as HEMA, since the drying necessary for proper intrusion of MMA into all of the connected space can create artefacts (Hellmuth et al., 2011).

6.2. Thermally initiated polymerisation of methacrylates in clay rock (article II)

Clay grains are typically found on the micrometre to nanometre scale. The pore apertures fall mostly within the nanometre range. Thus, any compound used in the tracer mixture should intrude effortlessly into the smallest pores. Fine-grained sedimentary rock was previously investigated using C-14-PMMA AG (Sammartino et al., 2001; 2002; Parneix et al., 2012; Robinet et al., 2015). These previous experiments relied on gamma irradiation to initiate the polymerisation reaction. However, MMA polymerisation has been performed through the thermal initiation in the interlayers of clay minerals (Blumstein, 1965); we, therefore, investigated the feasibility of using thermal initiation within the context of C-14-PMMA AG analysis of clay rocks. Due to the special properties of clay rock, we examined several issues related to application development for clay rock. Clay rock can change significantly following water saturation. Thus, initial studies focused on ascertaining the possibility of using water-soluble monomers. In this way, the sample would not necessarily require full drying. Here, we compared results from irradiation-initiated and thermally initiated polymerisation. Furthermore, clay rock tends to be softer than crystalline rock, making it more susceptible to coring damage. We, therefore, also investigated coring damage, since it is a highly possible artefact from sample preparation. Supporting porosity information was obtained via TGA and the literature (Pearson et al., 2003) on the sample material. Due to the heterogeneity of the sample material and the small scale of the mineral grains, we performed X-ray diffraction and SEM-EDS analyses.

As such, we produced an optimised polymerisation method to test the polymerisation of poly (HEMA-co-MMA) and different monomer ratios. We found that a mixture of 75% HEMA and 25% C-14-MMA with 0.5 wt% BPO yielded the best mechanical properties. The temperature programme developed was a gradient programme with an increase to 75°C over 20 h,

followed by a gradual cool down to 60° C during the subsequent 30 h. The temperature programme lasted 60 h in total. Opalinus clay samples were impregnated with this mixture of HEMA and C-14-MMA, the previously (article I) optimised mixture using only C-14-MMA and C-14-MMA polymerised using gamma irradiation. The Opalinus clay samples were successfully polymerised using all of these methods, producing autoradiographs on their basis. Figure 11 provides an example of the resulting C-14-PMMA autoradiographs. The impregnation appears thorough and we obtained reasonable values for the porosity results. We see, here, that a darker-coloured rim is visible in the surface scan and the sample autoradiograph.

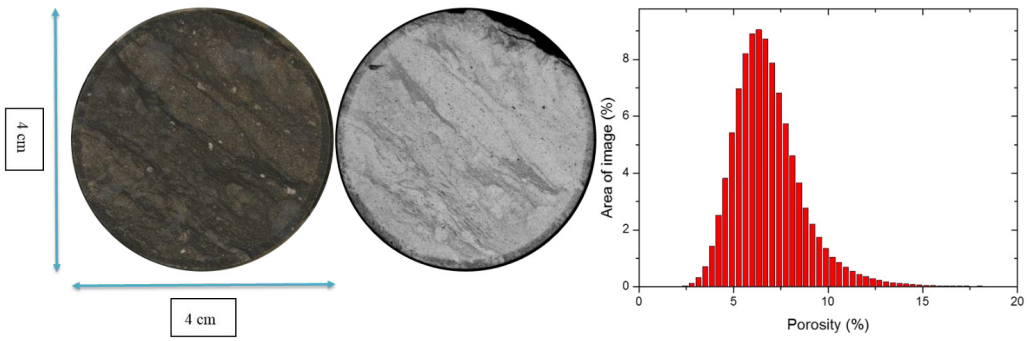

Figure 11. Surface scan (left), corresponding autoradiograph (centre) and porosity histogram (right) of clay rock sample impregnated with a mixture of 75% HEMA and 25% C-14-MMA. Figure from article II.

We also used SEM-EDS analyses to investigate the nature of this darker rim, the results of which appear in Figure 12. We see here that the morphology of calcium-containing minerals—in this sample, mostly calcite—changes near the sample edge. Along the edge, these calcium-containing minerals apparently fractured, since their average grain size is smaller. This same conclusion was reached through an analysis of both thermally polymerised samples that underwent the same sample preparation treatment. The width of the disturbed zone was different, however. The likely reason for this is the order on which the samples were drilled, since this along with the drilling time will affect the temperature of the drill. Because only two samples were drilled, we did not obtain sufficient material for statistical analysis. However, we aimed to determine the presence and the nature of a drilling artefact, which was successful.

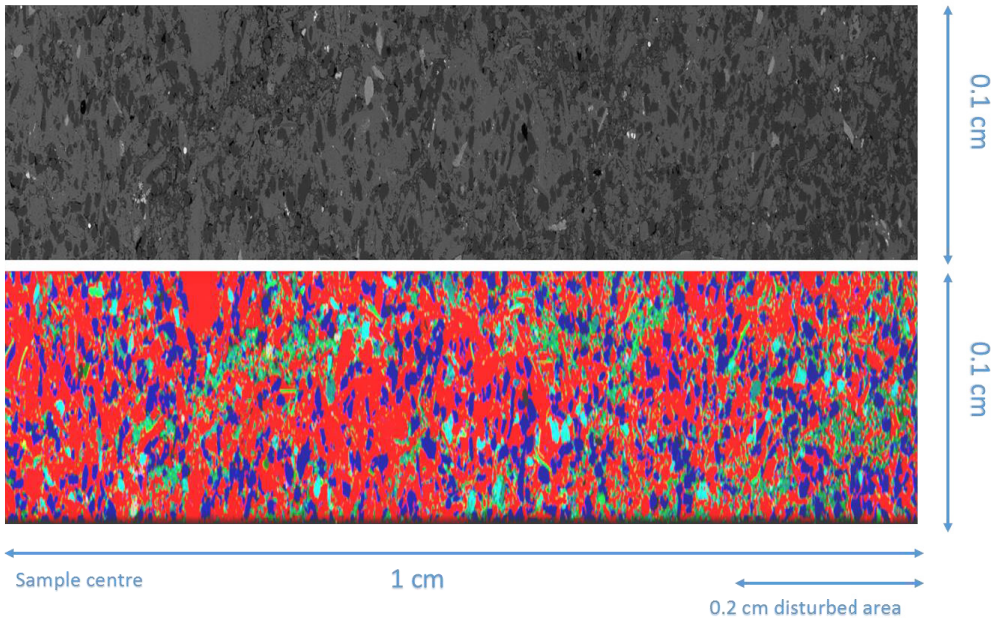

Figure 12. SEM BSE image (top) and corresponding SEM-EDS elemental map (bottom) from the clay rock sample impregnated with a mixture of 75% HEMA and 25% C-14-MMA. Figure from article II. Legend: red = calcium, blue = silicon, green = aluminium, blue + green = aluminium and silicon. XRD and SEM-EDS spot analyses were used to determine that calcium-bearing minerals were calcite, silicon-bearing minerals tended to be quartz and aluminium- and silicon-rich zones were filled with clay minerals.

Table 3 summarises the results from the tests conducted. We see here that the different monomer mixtures and initiation method combinations produce fairly similar porosity values. We did not, however, obtain precisely similar values, since the sample material represents heterogeneous rock. The results here are, however, in line with previous results for this rock type. In the reference sample, the disturbed zone was identified as consisting of more highly porous bands that happen to occur along the sample edges. This demonstrates that AG is required to visually distinguish a disturbed zone, since a profile trend can represent something else as well.

Table 3. Film autoradiography porosity results from samples impregnated with different monomer mixtures. The irradiation-initiated sample served as the reference sample. Data adapted from article II.

	Monomer mixtures		
	100% MMA	**100% MMA**	**75% HEMA, 25% MMA**
Initiation type	Irradiation	Thermal	Thermal
Mean total porosity	7.6	7.9	7.6
Mean disturbed zone porosity	14.0	11.8	11.9
Mean undisturbed zone porosity	7.2	6.8	6.3
Difference between total and undisturbed porosity (absolute % / relative %)	0.4% / 5.3%	1.1% / 16.2%	1.3% / 20.6%

Overall, these results show that similar porosity results could be obtained via thermal initiation and irradiation initiation on clay rock. A mixture composed of 75% HEMA and 25% C-14-MMA yielded similar results to those obtained using 100% MMA. In addition, these results approached previously obtained findings relying on the same technique for another set of Opalinus clay samples (Parneix et al., 2012). The mean porosity values fell along the lower limit of the spectrum of the porosity values obtained for Opalinus clay (Pearson et al., 2003). However, the samples studied here originated from carbonate-rich sandy facies, and previous work found that in Opalinus clay and Callovo-Oxfordian clay the porosity is inversely correlated with the carbonate and quartz concentrations (Houben et al., 2014; Robinet et al., 2015). Furthermore, the results here appear promising given the potential for in situ or saturated sample studies. We also found that drilling artefacts occur and can be easily distinguished through a visual inspection of the autoradiograph. Similarly, such artefacts result from the break-up of calcium-bearing grains (mostly calcite) in the disturbed zone.

6.3. Multiscale study of mineral porosity (article III)

In article III, we investigated the links between porosity and mineralogy on different scales. This work fell under the project investigating the retention properties of the Olkiluoto bedrock

or the REtention PROperties (REPRO) project (Voutilainen et al., 2014; Ikonen et al., 2015). Two long-term experiments are ongoing at the ONKALO repository site at Olkiluoto, both of which aim to increase our understanding of the retention properties of radionuclides (Voutilainen et al., 2014). Similar long-term experiments to understand the diffusion of radionuclides in bedrock have been undertaken at the Grimsel Test Site in Switzerland (Soler et al., 2015) and the Äspö Hard Rock Laboratory in Sweden (Widestrand et al., 2010). These experiments were supported by detailed rock matrix characterisation, while shorter scale experiments have also benefited from detailed information on the spatial distribution of porosity and mineralogy (Widestrand et al., 2007; Muuri et al., 2017). While in general the quality of the Olkiluoto bedrock is good and weak weathering is restricted to a few water-conducting fractures (Toropainen, 2012), in the geological history of Olkiluoto different alteration processes have taken place (Smellie et al., 2014) and these processes can result in local changes in the porosity. Altered crystalline rock tends to be more porous than unaltered rock. Furthermore, alteration can lead to the formation of clay minerals (Smellie et al., 2014), and the presence of clay minerals can change the retention properties of the rock matrix. Radioactive isotopes relevant to the final deposition of spent nuclear fuel, that are found as cations, appear to experience retention in clay minerals (Fuller et al., 2015; Mukai et al., 2016), while anions experience a variable amount of anion exclusion (Smith et al., 2004; Van Loon et al., 2007; Glaus et al., 2010).

The amount of these minerals is rather low in crystalline rock, making their characterisation challenging using bulk methods such as X-ray powder diffraction (XRD), since the sample matrix also contains many other minerals with strong diffraction patterns. These factors and many others contribute to the difficulty of reliably measuring the amount of clay minerals, especially if they are found in low abundance (Jozanikohan et al., 2016). XRD measurements tend to be semiquantitative in nature with a typical margin of error reaching ±3% (Hillier, 2000), a rather substantial margin when the relevant minerals are found primarily in low abundance in crystalline rock. In addition, bulk measurements do not yield any information on the spatial distribution of the minerals. SEM imaging combined with EDS, however, can provide localised information on elemental compositions, which in turn can be used to deduce mineral compositions. Thus, we decided to examine samples from the REPRO project in further detail. Initially, we examined the bulk porosities obtained via water gravimetry, argon

pycnometry and C-14-PMMA AG, as well as the mineralogical information provided by polarisation microscopy (Ikonen et al., 2015). From there, we created C-14-PMMA film autoradiographs and analysed the same surfaces using SEM-EDS. In this way, local porosities could be combined with local mineralogical information.

Based on the obtained film AG and SEM-EDS results, we conclusively found that areas of high porosity corresponded with areas of high alteration. While the rock is on average only slightly altered, areas of high alteration locally exist. In addition, SEM-EDS analyses illustrated in further detail the nature of the pore fillings found through polarisation microscopy (Ikonen et al., 2015).

In pegmatitic granite, we found that the pore network dominated by the grain boundary and intergranular porosity. This pore network exhibits a low tortuosity and is well-interconnected. Figure 13 provides an example of the spatial distribution of the porosity in pegmatitic granite.

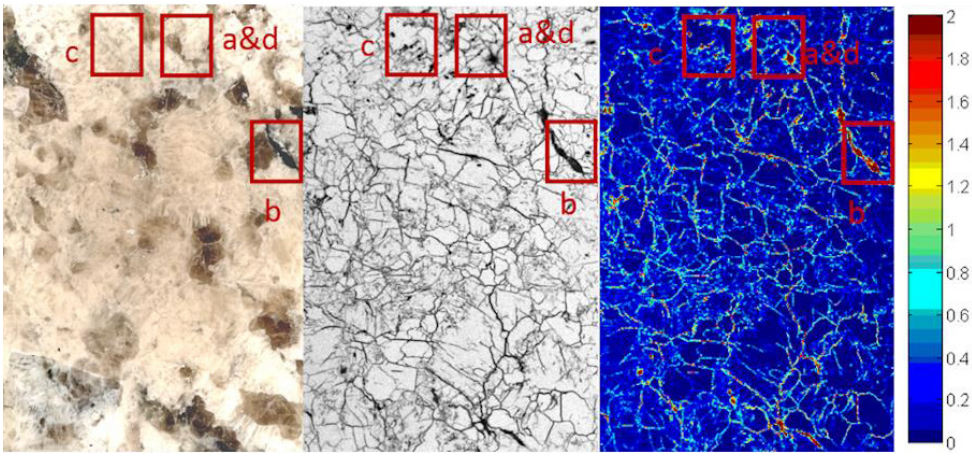

Figure 13. Surface scan (left), corresponding autoradiograph (centre) and corresponding porosity map (right) of Olkiluoto pegmatitic granite. The scale of the sample is 4 cm by 2.8 cm. Notation of areas a through d correspond to notation of areas a through d in Figure 14 (below) and are provided in more detail therein. Figure adapted from article III.

In pegmatitic granite, most pores were unfilled, although a notable number of the pores in plagioclase were filled with secondary muscovite. Some primary muscovite grains had also altered locally to illite and further to kaolinite. The measured pore apertures, either filled or unfilled, varied from 0.5 µm to 30 µm. Overall, we found that larger apertures associated with

the alteration processes, although some intergranular pores likely resulting from a brittle deformation were also quite wide. Figure 14 provides examples of the SEM imaging of pegmatitic granite.

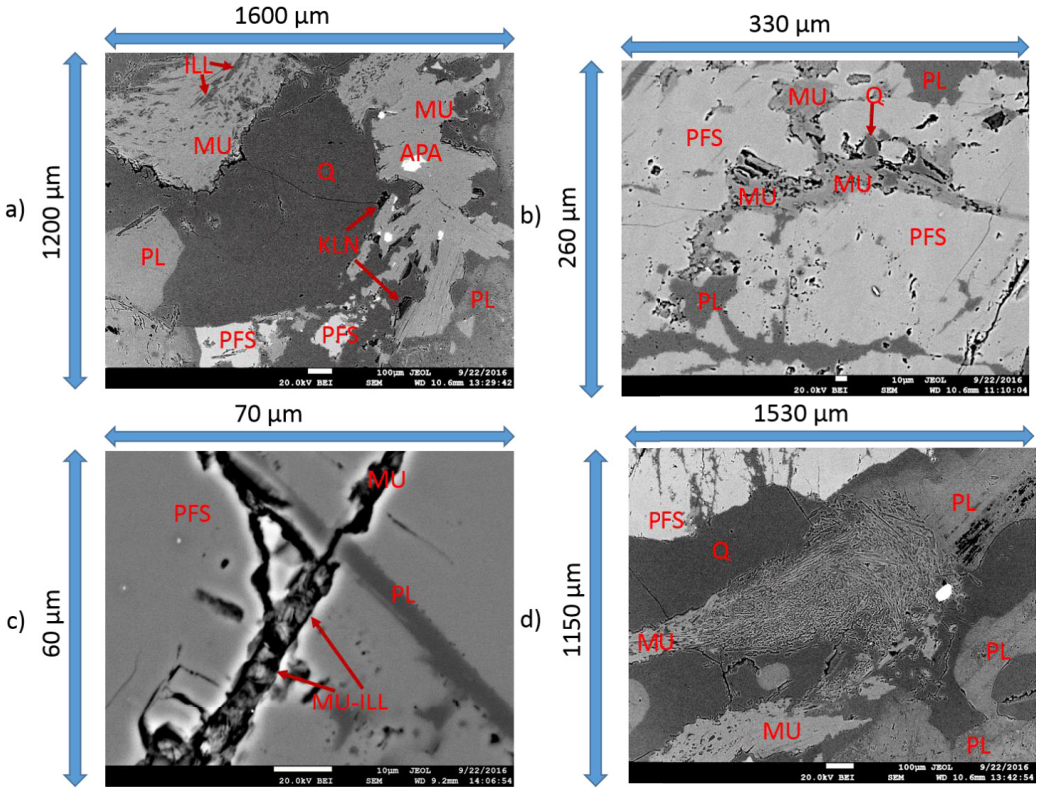

Figure 14. SEM-BSE imaging of Olkiluoto pegmatitic granite. Notations of areas a through d correspond to those used in Figure 13 (above). a) SEM-BSE image of quartz, K-feldspar, plagioclase and muscovite grains. b) Detailed view of a K-feldspar grain with a muscovitic alteration in perthite strings (albite). c) Muscovite/illite-filled intergranular fissure in K-feldspar with perthite intergrowths. d) Highly altered fine-grained phase between primary muscovite and plagioclase. Legend: APA = apatite, ILL = illite, MU = muscovite, MU-ILL = muscovite-illite mixture, PFS = K-feldspar, PL = plagioclase, Q = quartz. Figure adapted from article III.

In veined gneiss, the pore network is rather different from that of pegmatitic granite, being tortuous and more constricted. In Figure 15, we see few straight and wide pores and fissures on this scale, which are the mainstay of the pore network visible in Figure 13. Here, intragranular porosity forms the larger portion of the porosity. An example of the spatial distribution of porosity is presented in Figure 15.

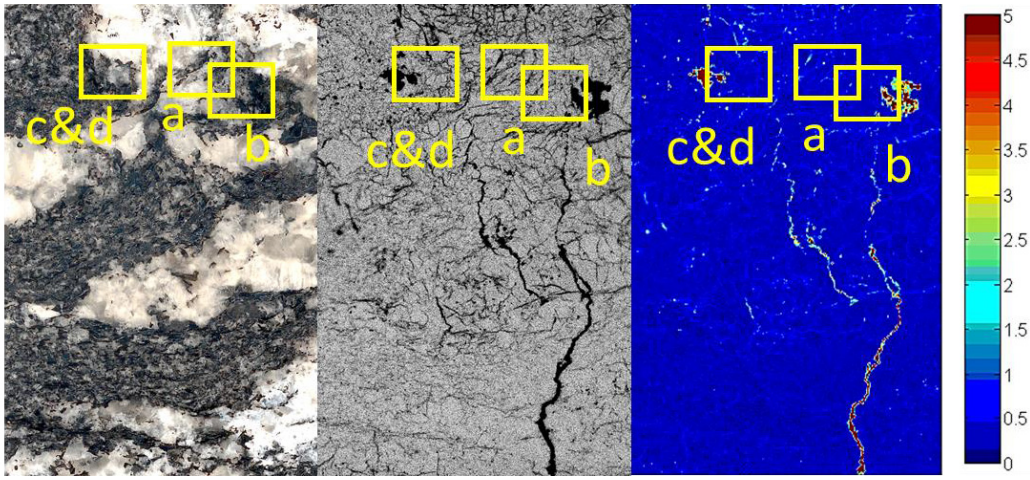

Figure 15. Surface scan (left), corresponding autoradiograph (centre) and the corresponding porosity map (right) of an Olkiluoto veined gneiss sample. The scale of the samples are 4 cm by 2.8 cm. Notations of the areas a through d correspond to those that appear in Figure 16 (below) are provided in more detail therein. Figure adapted from article III.

In veined gneiss, more filled pores were present. Cordierite represented the most altered mineral, altering to pinite to varying degrees. Pinite was typically found in vein-like formations that widened and interlinked increasingly alongside increasing pinitisation. Biotite appeared as primary biotite and as part of border (or b-pinite) composed of biotite and muscovite. In the interlamellar pores of primary biotite, kaolinite represented the most common filling. By contrast, b-pinite is composed of irregularly alternating layers of biotite and muscovite. The pore apertures for most grain boundary and intragranular pores reached 1 to 3 µm. In altered minerals, we found a wider range of apertures of 1 to 35 µm. Here, the alteration processes were connected to a wider range of apertures. Figure 16 provides examples of the SEM imaging results for veined gneiss.

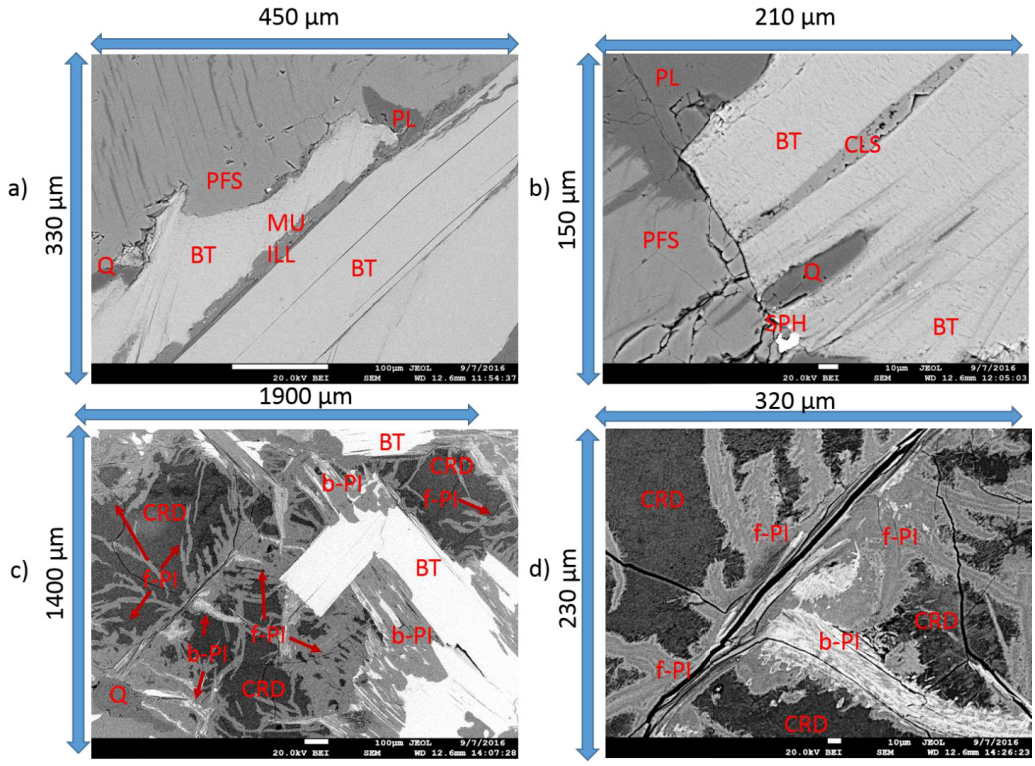

Figure 16. SEM-BSE imaging of an Olkiluoto veined gneiss sample. Notations of the areas a through d correspond to notations a through d used in Figure 15 (above). a) SEM-BSE image of biotite lamella with a thin (20 µm) muscovite flake with some illite present along the mineral border, probably as the alteration product. b) Biotite lamella with a 13-µm intragranular calcite filling. c) Biotite flakes surrounded by border-type pinite composed of muscovite and biotite, with a large cordierite grain on the left side partly altered to pinite beginning from the intragranular fissures. d) Close-up of the centre-left area from Figure 16 c) Highlight of both f-type pinite veins and b-type pinite grains. Legend: BT = biotite; CLS = calcite; CRD = cordierite; ILL = illite, MU = muscovite; b-PI = border-type pinite, f-PI = fissure-type pinite, PL = plagioclase, Q = quartz, SPH = sphalerite. Figure adapted from article III.

Table 4 summarises the pore characteristics of pegmatitic granite and veined gneiss obtained through SEM analysis. From this data, we find that grain boundary pores have a wider distribution in pegmatitic granite. Furthermore, intragranular pores have a wide distribution in both rock types, although in veined gneiss they tend to be more tortuous. Pegmatitic granite has a notable amount of transgranular fissures that cut through more than one mineral. Yet, this kind of porosity resulting from brittle fracturing is less evident in veined gneiss. Fillings were found in the pores of both rock types, but appear more commonly in veined gneiss. In

pegmatitic granite, fillings appeared in some of the plagioclase minerals. One common feature was that, in perthitised K-feldspar grains, the perthite strings had altered, becoming fine-grained muscovite. The primary muscovite grains of the pegmatitic granite were also partially altered to illite and, at times, further to kaolinite.

In veined gneiss, the pore fillings were primarily found in biotite and cordierite grains. Some instances of the intragranular pores of fractured quartz filling with kaolinite or other clay minerals also occurred. The interlamellar pores of biotite were nearly universally filled. In biotite, fillings consisted of kaolinite. Cordierite represented the most altered mineral of veined gneiss. In fact, cordierite almost always was present with at least some level of alteration and, in many cases, a high degree of alteration. Cordierite had altered to pinite, a heterogeneous assemblage of minerals that can take several forms and compositions. The two most common types consisted of border or b-pinite composed of biotite and muscovite, and fissure or f-pinite composed of an assemblage of clay minerals.

Table 4. Summary of pore characteristics for pegmatitic granite and veined gneiss by SEM. Data adapted from article III.

Pegmatitic granite			
Mineral	**Pore type**	**Pore size (µm)**	**Filling**
K-feldspar	Unconnected	2.0–6.0	No
K-feldspar	Transgranular	2.0–20.0	No
K-feldspar	Intragranular	1.0–5.0	Muscovite–illite
K-feldspar	Intragranular	0.5–1.5	No
K-feldspar / plagioclase	Intragranular	<1.0–5.0	No
K-feldspar / plagioclase	Intragranular	10.0–30.0	Muscovite
Primary muscovite	Intragranular	1.0–10.0	Illite
Quartz / K-feldspar	Grain boundary	1.0–2.0	No
Quartz / primary muscovite	Grain boundary	3.0–12.0	No
Veined gneiss			
Mineral	**Pore type**	**Pore size (µm)**	**Filling**
Biotite	Interlamellar	1.0–35.0	Kaolinite or muscovite-illite
Biotite	Interlamellar	13.0	Calcite
Biotite / quartz	Grain boundary	0.5–1.5	No
Biotite / K-feldspar	Grain boundary	0.5–1.5	No
Cordierite	Grain boundary	0.5–5.0	No
Cordierite	Intragranular	1.0–37.0	F-pinite
K-feldspar	Intragranular	0.5–2.0	No
K-feldspar / quartz	Grain boundary	2.0	No
Plagioclase	Unconnected	1.0	No
Plagioclase / quartz	Grain boundary	1.0–1.5	Kaolinite
Quartz	Intragranular	2.0	No
Quartz	Intragranular	1.0–20.0	Kaolinite or kaolinite–illite
Quartz	Unconnected	1.0	No
Quartz / sillimanite	Grain boundary	1.0	Kaolinite

From these results, we may draw the following conclusions regarding the effect of different rock types on the diffusion of radionuclides. It is quite possible that the pegmatitic veins within

the larger veined gneiss formations act as areas of faster transport due to the larger average pore apertures and diminished tortuosity. We found a clear effect of the pore structure in chloride diffusion experiments in veined gneiss and pegmatitic granite. Two-component modelling yielded the best fit to the experimental results (Sammaljärvi et al., 2017). In pegmatitic granite, the diffusion coefficients were notably different from each other, reflecting the diffusion in the large aperture–connected pores opposed to the slower diffusion in the smaller aperture and filled pores (Sammaljärvi et al., 2017). While veined gneiss can have a similar bulk porosity, its pores tend to be more tortuous with narrower grain boundary pores, decreasing the diffusion rates of elements. These grain boundary pores provide the shortest routes through the rock. Veined gneiss, however, possesses an abundance of small intragranular porosity. This porosity is either small in size or in effective aperture, since the bulk of the larger pores are filled. In this manner, the intragranular porosity can act as a kind of sink for any tracer passing through and doing so decreases the diffusivity.

Turning our attention to the tracer tests from the REPRO niche, it is possible that anion exclusion will affect the charged tracers. Anion exclusion phenomenon has been found to exist in clay mineral phases at varying strengths (Glaus et al., 2010). In veined gneiss, we found pinite and kaolinite in notable amounts. Pinite consists of minerals such as illite and smectite, which carry a strong anion exclusion potential. The laboratory scale through-diffusion tests of different tracers already demonstrated that chloride is affected by anion exclusion in veined gneiss, while such an effect was not observed in pegmatitic granite (Voutilainen et al., 2017a; 2017b). Thus, cationic tracers may experience enhanced retention in veined gneiss, while anionic tracers will diffuse faster through the rock matrix in the in situ experiments taking place at the REPRO site.

6.4. Contrast agent for X-ray tomography and scanning electron microscopy (article IV)

Article IV focused on the fixation of caesium chloride as a contrast agent for X-ray tomography and SEM image analysis. Many contrast agents such as mercury and Wood's metal are intruded into a sample via a pressure-driven process, which can create artefacts (Klaver et al., 2015). Here, we aimed to intrude a contrast agent via passive diffusion. Thus, we chose CsCl since it can be intruded in a saturated water solution; due to the high atomic number of

caesium, it can form a dense phase clearly visible with the techniques used. In these tests, we used samples taken from sites used in two in situ transport experiments: LTD from the Grimsel Test Site (Soler et al., 2015) and WPDE (Voutilainen et al., 2014) from ONKALO as a part of the REPRO project. Both of these locations host experiments that have used caesium as a tracer in the concentration resembling repository conditions. Results from the LTD experiment indicated that mineral heterogeneity is important for the retention of caesium. Therefore, information already exists regarding how caesium may behave in these types of rock, rendering them ideal test samples.

Therefore, we intruded a solution saturated with excess CsCl into the pores of Grimsel granodiorite and Olkiluoto veined gneiss samples. We then tested different immersion times to insure full intrusion. Because CsCl is water soluble, the fixation agent needs to be sparingly water soluble to prevent mobilisation of the contrast agent. MMA fulfils this condition. Thus, CsCl was then fixed in place by impregnating the samples with inactive MMA and subsequent thermally initiated polymerisation. Here, we used the polymerisation method developed during article I.

We found that CsCl was well-fixed in place and no notable amount was leached away during subsequent sample handling, despite the water solubility of CsCl. Immersion time in the CsCl solution produced no effect on the results, leading us to conclude that full immersion was already completed in the shortest timescale used. X-ray tomography was supported by the SEM–EDS analysis, whereby we noted a contrast improvement using both techniques. Figure 17 illustrates the contrast enhancement as seen using SEM imaging.

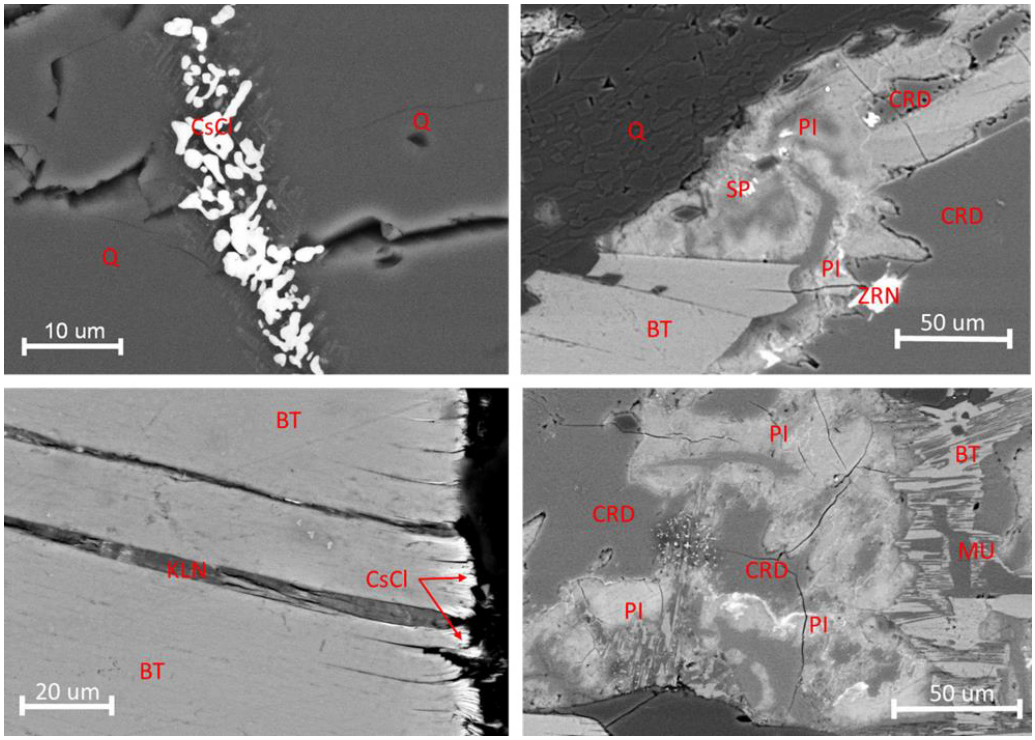

Figure 17. SEM–BSE imaging of Olkiluoto veined gneiss. Top left: Filled fissure in quartz (Q) grain. Top right: Pinitised (PI) cordierite (CRD). Bottom left: Unaltered biotite (BT) with kaolinite–filled (KLN) interlamellar pores, showing saw damage on the sample surface. Bottom right: Partially pinitised cordierite. Biotite and muscovite (MU) flakes are also present on the right-hand side of the image. Figure adapted from article IV.

We also compared SEM-EDS imaging and X-ray tomography, which is summarised in Figure 18. Here, we clearly see the CsCl phase in the elemental maps produced using SEM-EDS and in the X-ray tomography image.

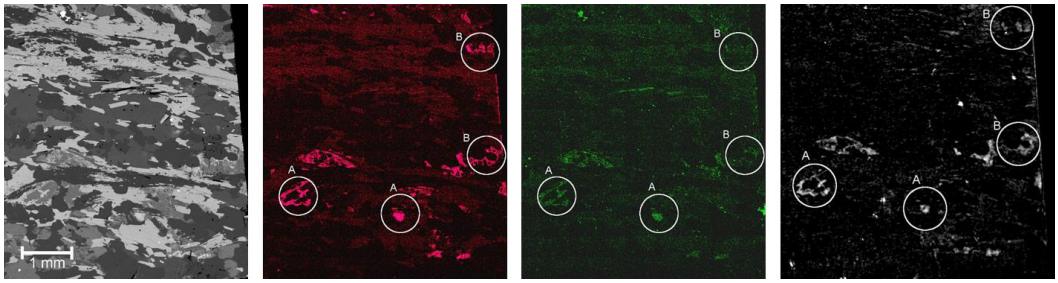

Figure 18. SEM–BSE image (far left), SEM-EDS Cs elemental map (middle left), SEM-EDS Cl elemental map (middle right) and X-ray tomographic image (right) of an Olkiluoto veined gneiss sample. Figure adapted from article IV.

The CsCl phases highlight the open pore space in both techniques. In pinitised cordierite, we found a higher abundance of Cs than Cl. Because pinite is composed of clay minerals such as illite and smectite, whereby anion exclusion possibly explains the disparity. Cs sorption into clay minerals may also have played a part as well, despite a saturation concentration that is not ideal for sorption. Some pore space was not highlighted, possibly resulting from a sample preparation artefact. This conclusion is supported by the fact that many of the unfilled pores appeared in brittle quartz minerals, which are prone to fracturing. Compaction artefacts, however, were not noted in the results, contrary to findings from pressure-intruded contrast agents (Klaver et al., 2015; Desbois et al., 2016), because the process used here did not require high pressures.

In future, however, research should attempt to improve our understanding of the kinetics and distribution mechanics of the contrast agent. In another study where the pores of illite were clogged with celestite, the precipitation conditions were strictly controlled (Chagneau et al., 2015). It is possible that better control over the precipitation process will further improve the contrast agent distribution.

In any case, this work demonstrates that the concept of filling pores with a contrast agent in principle works. We may conclude that these methods could be (1) used in an experiment with a shorter immersion time to obtain information on the intrusion speed. Furthermore, these methods could be (2) further developed by applying AG to provide complementary imaging of the spatial activity with a radioactive contrast agent and (3) applied to provide the spatial distribution of the elements used in in situ diffusion experiments such as LTD and TDE. In

addition, these methods may be (4) applied to construct a 3D map of the contrast agent distribution using tomography. This was accomplished previously using contrast agents such as Wood's metal (Pyrak-Nolte et al., 1995).

7. Conclusions and outlook

Our results expand the methodology and the scope of applications of the C-14-PMMA impregnation technique, while maintaining its robustness. Thermally initiated polymerisation produced similar porosity results to those previously obtained via irradiation-initiated polymerisation. This extends the potential use of the technique in normal laboratory conditions without needing exotic facilities such as a Co-60 source, and reducing experiment times, since the irradiation facility might not be available for the dose rate needed for polymerisation within a reasonable time frame. Thermally initiated polymerisation, by contrast, can be accomplished in a normal laboratory setting and overnight. Furthermore, we can reasonably assume that broadly similar reaction conditions are suitable for use with other thermally degrading radical initiators. Overall, we noted no differences in the autoradiographs produced via the tracer polymerised using different methods. This held true for all of materials studied including brick, Grimsel granodiorite, Opalinus clay, Olkiluoto veined gneiss and Olkiluoto pegmatitic granite.

The possibility of carrying out in situ experiments within repositories, where complete drying of the sample material is difficult, relies on using water-soluble monomers as impregnants. We tested these monomers and their mixtures, and found results comparable to those obtained via a simpler mixture of one impregnant and a radical initiator. Therefore, working with partially or fully water-saturated rock samples should also be further investigated. Clay rock represents a good example of a material with a different structure depending on the saturation state. Soil represents another such material. The properties of these materials strongly depend on their saturation state. Thus, being able to fix them into plastic and studying their properties at different saturation states would prove useful.

Furthermore, in article III, we combined the spatial distribution of porosity on hand specimen–scale samples provided through C-14-PMMA AG and the local mineral composition on a micrometre scale provided through SEM imaging. Combining this information illustrated the relationship between macroscopic rock porosity and the microscopic structure. In this study, we selected the areas of interest, although a more wide-scale mineralogical mapping could be carried out in future. In addition, in article II, we combined centimetre-scale AG with SEM imaging of the same area with suitable magnification, a combination that should become routine in future. The measurements of the pore apertures helped explain some of the results

already obtained from matrix diffusion experiments. The clay mineral findings in the pore structure of the Olkiluoto bedrock may have implications for the modelling of matrix diffusion in bedrock, since the cations often experience strong retention in clay minerals, while anions are excluded from the pore spaces of certain clay minerals. In particular, long-term experiments at Olkiluoto will benefit from an improved understanding of the rock matrix.

The CsCl fixation study detailed in article IV demonstrated that other tracers could be fixed via impregnation using MMA. We found that, while a contrast agent compound filling the pores was already present, complete infiltration by MMA could be achieved. PMMA was, therefore, capable of holding all of the tracer in place. This study should be repeated with other tracer compounds, particularly those relevant to the final deposition of spent nuclear fuel. In addition, repeating the study with isotopes such as ^{134}Cs to simultaneously obtain an autoradiographic image of the Cs distribution may also prove interesting.

While this study focused primarily on natural materials, the methods developed could easily be applied to porosity analyses of man-made materials, such as cement and concrete. The interfaces between man-made and natural materials also represent another area for future investigations.

The future development of C-14-PMMA AG does not just involve new materials, but also applies to taking advantage of technological developments related to it and other techniques. One promising avenue lies in combining it with stimulated emission depletion microscopy (STED)–based analysis to produce nanoscopy, thus complementing the porosity distribution information. This could be particularly useful for altered areas of crystalline and clay rock, which have very small pore apertures. Another important development lies in filmless AG provided by parallel gas chamber detector systems, such as Le Beaver, wherein the local activity is directly measured from the sample. Thus, the development process is simplified by the omission of films or imaging plates which must be exposed and developed. This approach could lead to fewer uncertainty factors in the measurement of porosity.

8. References

Abell A.B., Willis K.L., Lange D.A. 1999. Mercury Intrusion Porosimetry and Image Analysis of Cement-Based Materials. Journal of Colloid and Interface Science, 211, 39-44.

Andra. 2005. Andra research on the geological disposal of high-level long-lived radioactive waste – Results and perspectives. Dossier 2005, Andra Report Series.

Anotvitz L.M. & Cole D.R. 2015. Characterization and analysis of porosity and pore structures. Reviews in Mineralogy & Geochemistry. 80, 61-164.

Appelo C.A.J., Van Loon L.R., Wersin P. 2010. Multicomponent diffusion of a suite of tracers /HTO, Cl, Br, I, Na, Sr, Cs) in a single sample of Opalinus Clay. Geochimica et Cosmochimica Acta, 74, 1201-1219.

Autio J., Siitari-Kauppi M., Timonen J., Hartikainen K., Hartikainen J. 1998. Determination of the porosity, permeability and diffusivity of rock in the excavation-disturbed zone around full-scale deposition holes using the C-14-PMMA and He-has methods. Jounrla of Contaminant Hydrology, 35, 19-29.

Baraka-Lokmane S. 2002. A new resin impregnation technique for characterizing fracture geometry in sandstone cores. International Journal of Rock Mechanics & Mining Sciences, 39, 815-823.

Barnes C.E. 1945. Mechanism of Vinyl Polymerization. I. Role of Oxygen. Journal of American Chemical Society, 67(2), 217-220.

Baskin D.G. & Wimpy T.H. 1989. Calibration of [^{14}C] plastic standards for quantitative autoradiography of [^{125}I] labeled ligands with Amersham Hyperfilm β-max. Neuroscience Letters, 104,171-177.

Beall F.C. & Witt A.E. 1972. Polymerization of methyl methacrylate by heat-catalyst and gamma-irradiation methods. Wood & Fiber, 4(3), 179-184.

von Berlepsch T. & Haverkamp B. 2016. Salt as a Host Rock for the Geological Repository for Nuclear Waste. Elements, 12, 257-262.

Blumstein A. 1965. Polymerization of Adsorbed Monolayers. II. Thermal degradation of the inserted polymer. Journal of Polymer Science: Part A, 3, 2665-2672.

Bradbury, M.H. and Green, A. 1986. Investigations into the factors influencing long range matrix diffusion rates and pore space accessibility at depth in granite. Journal of Hydrology, 89: 123-139.

Brad K.K., Davis C.R., Shervais J.W., Janecke S.U., Evans J.P. 2015. Composition, Alteration and Texture of Fault-Related Rocks from Safod Core and Surface Outcrop Analogs: Evidence for Deformation Processes and Fluid-Rock Interactions. Pure and Applied Geophysics, 172, 1053-1078.

Bucher K. & Grapes R. 2011- Petrogenesis of metamorphic rocks. 8th edition. Springer-Verlag Berlin Heidelberg.

Bugani S., Camaiti M., Morselli L., Van de Casteele E., Janssens K. 2007. Investigation on porosity changes of Lecce stone due to conservation treatments by means of x-ray nano- and improved micro-computed tomography: preliminary results. X-ray Spectrometry, 36, 316-320.

Byegård J., Johanson H., Skålberg M., Tullborg E.-L. 1998. The interaction of sorbing and non-sorbing tracers with different Äspö rock types. SKB Technical Report TR-98-18. SKB.

Byerlee J.D. Brittle-Ductile Transition in Rocks. Journal of Geophysical Research, 73(14), 4741-4750.

Casimiro M.H., Botelho M.L., Leal J.P., Gil M.H. 2005. Study on chemical, UV and gamma radiation-induced grafting of 2-hydroxyethyl methacrylate onto chitosan. Radiation Physics and Chemistry, 72, 731-735.

Chagneau A., Tournassat C., Steefel C.I., Bourg I.C., Gaboreau S., Esteve I., Kupcik T., Claret D., Schäfer T. 2015. Complete restriction of 36Cl- diffusion by celestite precipitation in densely compacted illite. Environmental Science and Technology Letters, 2, 139-143.

Coats A.W. & Redfern J.P. 1963. Thermogravimetric Analysis: A review. Analyst, 88, 906-924.

Darot M. & Reuschle T. 1999. Direct Assessment of Wood's Metal Wettability on Quartz. Pure and Applied Geophysics, 155, 119-129.

Davenport A.P. & Hall M.D. 1988. Comparison between brain paste and polymer [^{125}I] standards for quantitative receptor autoradiography. Journal of Neuroscience Methods, 25, 75-82.

Davy C.A., Nguyen Kim T., Song Y., Troadec D., Blanchenet A.-M., Adler P.M. 2017. Understanding fluid transport through the multiscale pore network of a natural shale. EPJ Web of Conferences, Powders & Grains 2017 – 8th International Conference on Micromechanics on Granular Media, 140, 12016.

Day-Stirrat R.J., Flemings P.B., You Y., Aplin A.C., van der Pluijm B.A. 2012. The fabric of consolidation in Gulf of Mexico mudstones. Marine Geology, 295-298, 77-85.

De Witte E., Huget P., Van den Broeck P. 1977. A comparative study of three consolidation methods on limestone. Studies in Conservation, 22, 190-196.

DECC (Department of Energy and Climate Change). 2014. Implementing Geological Disposal – A Framewrok for the long-term management of higher activity radioactive waste. Department of Energy and Climate Change Policy Paper, 14D/235.

Degueldre C., Pleinert H., Maguire P., Lehman E., Missimer J., Hammer J., Leenders K., Böck H., Townsend D. 1996. Porosity and pathway determination in crystalline rock by positron emission tomography and neutron radiography. Earth and Planetary Science Letters, 140, 213-225.

Desbois G., Hemes S., Laurich B. Houben M., Klaver J., Höhne D., Urai J.L., Viffiani G., Bésuelle P. 2016. Investigation of microsctructures in naturally and experimentally deformed reference clay rocks using innovative methods in scanning electron microscopy. The Clay Minerals Society Workshop Lectures Series, 21, 1-14.

Dewhurst D.N., Aplin A.C., Sarda J.-P., Yang Y. 1998. Compaction-driven evolution of porosity and permeability in natural mudstones: An experimental study. Journal of Geophysical Research,103(B1), 651-661.

Donnard J., Berny R., Carduner H., Leray P., Morteau E., Provence M., Servagent N., Thers D. 2009a. The micro-pattern gas detector PIM: A multi-modality solution for novel investigations in functional imaging. Nuclear Instruments and Methods in Physics Research A, 610, 158-160.

Donnard J., Thers D., Servagent N., Luquin L. 2009b. High Spatial Resolution in β-imaging with a PIM device. IEEE Transactions on Nuclear Science, 56, 197-200.

Dultz S., Behrens H., Simonyan A., Kahr G., Rath T. 2006. Determination of porosity and pore connectivity in feldpars from soils of granite and saprolite. Soil Science, 171(9), 675-694.

Ewing R.C. 2015. Long-term storage of spent nuclear fuel. Nature Materials, 14, 252-257.

Emmanuel S., Anovitz L.M., Day-Stirrat R.J. 2015. Effects of Coupled Chemo-Mechanical Processes on the Evolution of Pore-Size Distributions in Geological Media. Reviews in Mineralogy & Geochemistry, 80, 45-60.

Fecchio B.D., Valandro S., Neumann M.G., Cavalheiro C.C.S. 2016. Thermal decomposition of Polymer/Montmorillonite nanocomposites synthesized in situ on a clay surface. Journal of Brazilian Chemical Society, 27(2), 278-284.

Fichet P., Bresson F., Leskinen A., Goutelard F., Ikonen J. Siitari-Kauppi M. 2012. Tritium analysis in building dismantling process using digital autoradiography. Journal of Radioanalytical and Nuclear Chemistry, 291, 869-875.

Forberg S., Odeblad E., Söremark R., Ullberg S. 1964. Autoradiography with Isotopes Emitting Internal Conversion Electrons and Auger Electrons. Acta Radiologica: Therapy, Physics, Biology, 2(4), 241-262.

Formoso M.L.L. 2006. Some topics on geochemistry of weathering. a review. Annals of the Brazilian Acedemy of Sciences, 78(4), 809-820.

Fossen H., Schultz R.A., Shipton Z.K., Mair K. Deformation bands in sandstone: a review. Journal of the Geological Society, London, 164, 755-769.

Friel J.J. 2003. X-ray and image analysis in electron microscopy.2nd edition. Priceton Gamma-Tech, New Jersey, USA. ISBN. 0-9641455-1-0.

Fuller A. J., Shaw S., Ward M. B., Haigh S. J., Mosselmans J. F. W., Peacock C. L., Stackhouse S., Dent A. J., Trivedi D., Burke I. T. 2015. Caesium incorporation and retention in illite interlayers. Applied Clay Science 108, 128-134.

Gaboreau S., Prêt D., Tinseau E., Claret F., Pellegrini D., Stammose D. 2011. 15 years on in situ cement-argillite interaction from Tournemire URL: Charcterisation of the multi-scale spatial heterogeneities of pore space evolution. Applied Geochemistry, 26, 2158-2171.

Gao F. 2004. Clay/polymer composites: the story. Materials Today, 7(11), 50-55.

García-Gutíerrez M., Cormenzana J.L., Missana T., MIngarro M., Martín P.L. 2006. Large-scale laboratory diffusion epxriments in clay rocks. Physics and Chemistry of the earth, 31, 523-530.

Glaus, M.A., Frick, S., Rossé, R. & Van Loon, L.R. (2010) Comparative study of tracer diffusion of HTO, Na-22, Cl-36 in compacted kaolinite, illite and montmorillonite. Geochimica et Cosmochimica Acta74, 1999-2010.

Giesche H. 2006. Mercury porosimetry: a general (practical) overview. Particle & Particle Systems Characterization, 23, 1-11.

Gould R.F. (ed.). 1967. Irradiation of Polymers. Advances in Chemistry Series. American Chemical Society, Washington D.C., USA.

Gowd T.N. & Rummel F. 1980. Effect of confining pressure on the fracture behaviour of a porous rock. International Journal of Rock Mechanics and Mining Sciences & Geomechanics Abstracts. 17(4), 225-229.

Grambow B. 2016. Geological Disposal of Radioactive Waste in Clay. Elements, 12, 239-245.

Grubbs R.B. 2011. Nitroxide-Mediated Radical Polymerization: Limitations and Versatility. Polymer Reviews, 51, 104-137.

Gu C., Wang D., Wang X., Huang Y., Zhen Z., Liu X. 2002. Bulk Polymerization of Methyl Methacrylate Initiated by High Intensity Ultrasonic Irradiation and ESR Study. Journal of Applied Polymer Science, 86, 1731-1735.

Günzler F., Wong E.H.H., Koo S.P.S., Junkers T., Barner-Kowollik C. 2009. Quantifying the Efficiency of Photoinitiation Processes in Methyl Methacrylate Free Radical Polymerization via Electrospray Ionization Mass Spectrometry. Macromolecules, 42, 1488-1493.

Hasegawa S. & Nishimura N. 1960. Studies on Organic Peroxides. V. Decomposition of Benzoyl peroxide by iron(II). Studies on Organic Peroxides, V, 775-779.

Hedin A. & Olsson O. Crystalline Rock as a Repository for Swedish Spent Nuclear Fuel. Elements, 12, 247-252.

Hellmuth K.-H. & Siitari-Kauppi M. 1990. Investigation of the porosity of rocks. Impregnation with 14C-polymethylmethacrylate (PMMA), a new technique. STUK-B-VALO 63.

Säteilyturvakeskus. The Finnish Government Printing Centre, Helsinki, Finland. ISBN: 951-47-3949-3.

Hellmuth K.-H., Siitari-Kauppi M., Lindberg A. 1993. Study of porosity and migration pathways in crystalline rock by impregnation with C-14-polymethylmethacrylate. Journal of Contaminant Hydrology, 13, 403-418.

Hellmuth K.-H., Lukkarinen S., Siitari-Kauppi M. 1994. Rock matrix studies with carbon-14-polymethylmethacrylate (PMMA); method development and applications. Isotopenpraxis Environmental Heatl Studies. 30, 47-60.

Hellmuth K.-H., Klobes P., Meyer K., Böhl-Kuhn B., Siitari-Kauppi M., Hartikainen J., Hartikainen K., Timonen J. 1995. Matrix retardation studies: size and structure of the accessible pore space in fresh and altered crystalline rock. Zeitschrift für Geologische Wissenschaften, 23 (5/6), 691-706.

Hellmuth K.H., Siitari-Kauppi M., Kolbes P., Meyer K., Goebbels J. 1999. Imaging and Analyzing Rock Porosity by Autoradiography and Hg-porosimetry/X-ray Computermicrotomography – Applications. Physics & Chemistry of the Earth (A), 24(7), 569-573.

Hellmuth K.-H., Siitari-Kauppi M., Sardini P. 2011. Development work 2010-2011. For implementing the technical platform (WP 3), the development of the saturation technique (WP 4), and applications (WP 5). POSINAM Report, Marie Curie IAPP project number 230635.

Hellmuth K.-H., Siitari-Kauppi M., Arvela H., Lindberg A., Fonteneau L., Sardini P. 2017. Radon emanation from fresh, altered and disturbed granitic rock characterized by ^{14}C-PMMA impregnation and autoradiography. Applied Radiation and Isotopes, 127,195-208.

Hildenbrand A. & Urai J.L. 2003. Investigation of the morphology of pore space in mudstones – first results. Marine and Petroleum Geology, 20, 1185-1200.

Hirth G. & Tullis J. 1989. The Effects of Pressure and Porosity on the Micromechanics of the Brittle-Ductile Transition in Quartzite. Journal of Geophysical Research, 94(B12), 17825-17838.

Holland M., Urai J.L., van der Zee W., Stanjek H., Konstanty J. 2006. Fault gouge evolution in highly overconsolidated claystones. Journal of Structural Geology, 28, 323-332.

Houben, M.E., Desbois, G., Urai, J.L. 2014. A comparative study of representative 2D microstructures in Shaly and Sandy facies of Opalinus clay (Mont Terri, Switzerland) inferred from BIB-SEM and MIP methods. Marine and Petroleum Geology 49, 143–161.

Hölttä P., Siitari-Kauppi M., Huittinen N., Poteri A. 2007. Determination of Matrix Diffusion Properties of Granite. Material Research Society Symposium Proceedings, 985, 557-562.

International Society for Rock Mechanics, Commission on standardization of laboratory and field tests, 1979. Suggested methods for determining water content, porosity, density, absorption and related properties and swelling and slake-durability index properties. International Journal of Rock Mechanics, Mining Science & Geomechanical Abstracts 16, 141–156.

Jamtveit B., Kobchenko M., Austrheim H., Malthe-Sørensen, Røyne A., Svensen H. 2011. Porosity evolution and crystallization-driven fragmentation during weathering of andesite. Journal of Geophysical Research, 116(B12), B12204.

Jamtveit B. & Hammer Ø. 2012. Sculpting of Rocks by Reactive Fluid. Geochemical Perspectives, 1 (3), 341-481.

Jeong J., Sardini P., Ramézani H., Siitari-Kauppi M., Steeb H. 2013. Modeling of the induced chemo-mechanical stress through porous cement mortar subjected to CO2: Enhanced micro-dilatation theory and C-14-PMMA method. Computational Materials Science, 69, 466-480.

Jeong J., Ramézani H., Sardini P., Kondo D., Ponson L., Siitari-Kauppi M. 2015. Porous media modeling and micro-structurally motivated material moduli determination via the micro-dilatation theory. European Physical Journal Special Topics, 223, 1805-1816.

Jozanikohan G., Sahabi F., Norouzi G.H., Memarian H., Moshiri B. 2016. Quantitative analysis of the clay minerals in the Shurijeh Reservoir Formation using combined X-ray analytical techniques. Russian Geology and Geophysics, 57, 1048-1063.

Kamineni D.C., Ticknor K.V., Vandengraad T.T. 1986. Occurence, composition and radionuclide sorption characteristics of illite from a fractured granite pluton, Southern Manitoba, Canada. Clay MIneral, 21, 909-924.

Kaufmann J.2009. Characterization of Pore Space of Cement-Based Materials by Combined Mercury and Wood's Metal intrusion. Journal of American Ceramics Society, 92(1), 209-216.

Keller L.M., Holzer L., Wepf R., Gasser P. 2011. 3D geometry and topology of pore pathways in Opalinus clay: Implications for mass transport. Applied Clay Science, 52, 85-95.

Keller L.M., Schuetz P., Erni R., Rossell M.D., Lucas F., Gasser P., Holzer L. 2013. Characterization of multi-scale microstructural features in Opalinus Clay. Microporous and Mesoporous Materials, 170, 83-94.

Kelokaski M., Siitari-Kauppi M., Sardini P., Möri A., Hellmuth K.-H. 2006. Characterisation of pore space geometry by C-14-PMMA impregnation – development work for in situ studies. Journal of Geochemical Exploration, 90, 45-52.

Kemppainen M., Oila E., Siitari-Kauppi M., Sardini P., Hellmuth K.-H. 2001. Surveying for Migration Pathways in the Granitic Rock Using Nuclear track Detectors, Autoradiography and Digital Image Analysis as an Aid To Construct the Basis for Heterogeneous Diffusion Modeling. Material Research Society Symposium Proceedings, 663, 999-1006.

Klaver J., Hemes S., Houben M., Desbois G., Radi Z., Urai J.L. 2015. The connectivity of pore space in mudstones: insights from high-pressure Wood's metal injection, BIB-SEM imaging, and mercury intrusion porosimetry. Geofluids, 15(4), 577-591.

Klobes P., Riesemeier H., Meyer K., Goebbels J., Hellmuth K.-H. 1997a. Rock porosity determination by combination of X-ray computerized tomography with mercury porosimetry. Fresenius Journal of Analytical Chemistry, 357, 543-547.

Klobes P., Riesemeier H., Meyer K., Goebbels J., Siitari-Kauppi M., Hellmuth K.-H. Investigation of rock samples using X-ray-microcomputer-tomography before and after mercury intrusion porosimetry. Material Research Society Symposium Proceedings. 465, 863-870.

Knoll G.F. 2010. Radiation Detection and Measurement. 4th edition, John Wiley & Sons, Inc. USA. ISBN: 978-0-470-13148-0.

Koç Z., Çelik M., Önal M., Sarıkaya Y., Mogulkoc Y. 2013. Preparation and characterization of poly (2-hydroxy ethyl methacrylate)/Na-montmorillonite intercalated nanocomposites. Journal of Polymer Engineering, 33(1), 27-32.

Kornprobst J. 2002. Metamorphic rocks and their geodynamic significance: petrological handbook. Kluwer Acedemic Publishers.

Kranz R.L. 1983. Microcracks in rocks: a review. Tectonophysics, 100, 449-480.

Kuva J., Siitari-Kauppi M., Lindberg A., Aaltonen I., Turpeinen T., Myllys M., Timonen J. 2012. Microstructure, porosity and mineralogy around fractures in Olkiluoto bedrock. Engineering Geology, 139-140, 28-37.

Kuva J., Voutilainen M., Lindberg A., Parkkonen J., Siitari-Kauppi M., Timonen J. 2015. Pore and mineral structure of rock using-nanotomographic imaging. Material Research Society Symposium Proceedings, 1744, 235-240.

Kuva J. 2016. Tracer migration in crystalline rock – Application to geological barriers of nuclear waste storage. Academic dissertation of the degree of Doctor of Philosophy. Department of Physics, University of Jyväskylä. Research Report 2/2016.

Kyser (ed.). 2000. Fluids and Basin Evolution, Chapter: 4, 63-92. Mineralogical Association of Canada. ISBN: 0-921294-28-x

Kämäräinen E.-L., Haaparanta M., Siitari-Kauppi M., Koivula T., Lipponen T., Solin O. (2006) Analysis of 18F-labelled synthesis products on TLC plates: comparison of radioactivity scanning, film autoradiography, and a phosphoimaging technique, Applied Radiation and Isotopes 64. 1043-1047.

Lai J., Wang G., Chai Y., Xin Y., Wu Q., Zhang X., Sun Y. Deep burial diagenesis and reservoir quality evolution of high-temperature, high pressure sandstones. Examples from Lower Cretaceous Bashijiqike Formation in Keshen area, Kuqa depression, Tarim basin of China. AAPG Bulletin, 101(6), 829-862.

Lalan P., Dauzères A., De Windt L., Bartier D., Sammaljärvi J., Barnichon J.-D., Techer I., Detilleux V. 2016. Impact of a 70°C temperature on an ordinary Portland cement paste/claystone interface. An in situ experiment. Cement and Concrete Research, 83, 164-178.

L'Annunziata (ed). 2003. Handbook of Radioactivity Analysis. 2nd edition.Pahes 1063-1127.

Langhals H. & Oginski B. 2008. Electron beam curing with glycerol methacrylate. Journal of Polymer Science part A: Polymer Chemistry, 46, 6660-6663.

Laubach S.E. & Ward M.E. Diagenesis in porosity evolution of opening-mode fractures, Middle Triassic to Lower Jurassic La Boca Formation, NE Mexico. Tectonophysics, 419, 75-97.

Laverov N.P., Yudintsev S.V., Kochkin B.T. Malkovsky V.I. 2016. The Russian Strategy of using Crystalline Rock as a Repository for Nuclear Waste. Elements, 12, 253-256.

Lehtinen M., Nurmi P., Rämö T. (ed.). Suomen Kallioperä -3000 vuosimiljoonaa. Helsinki, Suomen Geologinen Seura ry. ISBN: 952-90-9260-1. (In Finnish).

Leskinen A., Penttinen L., Siitari-Kauppi M., Alanso U., Garcia-Gutierrez M., Missana T., Patelli A. 2007. Determination of granites' mineral specific porosities by PMMA method and FESEM/EDAX. Material Research Society Symposium Proceeding, 985.

Liu G.-D., Zhang L.-C., Qu X.-W., Wang B.-T., Zhang Y. 2003. Tentative study on kinetics of bulk polymerization of methyl methacrylate in presence of montmorillonite. Journal of Applied Polymer Science, 90, 3690-3695.

Lloyd G.E. 1987. Atomic number and crystallographic contrast images with the SEM: a review of backscattered electron techniques. Mineralogical Magazine, 51, 3-19.

Lucia F.J. 2007. Carbonate Reservoir Characterization. An Integrated Approach. Springer. ISBN: 978-3-540-72740-8.

Lähdemäki T., Kelokaski M., Siitari-Kauppi M., Voutilainen M., Myllys M., Turpeinen T., Timone J., Mateos F., Montoto M. 2007. Characterizing Low-Permeable Granitic Rock From micrometer to Centimeter Scale: X-ray Microcomputed Tomography, Confocal laser Scanning Microscopy and ^{14}C-PMMA Method. Material Research Society Symposium Proceedings. 985, 0985-NN11-18.

Malhotra S.L., Parikh K.K., Blumstein A. 1971. VII. Influence of the exchangeable cation on the polymerization rate of the methylmethacrylate monolayers adsorbed on montmorillonite. Journal of Colloid and Interface Science, 41 (2), 318-327.

Matyjaszewski K. 2012. Atom Transfer Radical Polymerization (ATRP): Current Status and Future Pespectives. Macromolecules, 45, 4015-4039.

Mazurier A., Sardini P., Rossi A.M., Graham R.C., Hellmuth K.-H., Parneix J.-C., Siitari-Kauppi M., Voutilainen M., Caner L. 2016. Development of a fracture network in crystalline rocks

during weathering: Study of Bishop Creek chronosequence using X-ray computed tomography and C-14-PMMA impregnation method. The Geological Society of America Bulletin, 128, 1423-1438.

Mazzullo. S.J. 2004. Overview of Porosity Evolution in Carbonate Reservoirs. Search & Discovery, article #40134.

Melnyk, T.W., Skeet, A.M.M. 1986. An improved technique for determination of rock porosity. Canadian Journal of Earth Science 23, 1068–1074.

Mielenz R.C., Schieltz N.C. King M.E. 1953. Thermogravimetric Analysi of Clay and Clay-like Minerals. Clays and clay minerals : proceedings of the second National Conference on clays and clay minerals, University of Missouri, Columbia, Missouri, October 15-17, 1953, pages 285-314.

Miller J.A. & Zahniser N.R. 1987. The use of ^{14}C-labeled tissue paste standards for the calibration of 125I-labeled ligands in quantitative autoradiography. Neuroscience Letters, 81, 345-350.

Miller J.A. 1991. The calibration of ^{35}S or ^{32}P with ^{14}C-labeled brain paste or ^{14}C-plastic standards for quantitative autoradiography using LKB Ultrofilm or Amersham Hyperfilm. Neuroscience Letters, 121, 211-214.

Moad G., Rizzardo E., Thang S.H. 2013. RAFT Polymerization and Some of its applications. Chemistry – An Asian Journal, 8, 1634-1644.

Morad S., El-Ghali M.A.K., Caja M.A., Sirat M., Al-Ramadan K., Mansurbeg H. 2009. Hydrothermal alteration of plagioclase in granitic rocks from Proterozoic basement of SE Sweden. Geological Journal, 45(1), 105-116.

Montheard J.-P., Chatzopoulos M., Chappard D. 1992. 2-Hydroxyethyl Methacrylate (HEMA): Chemical Properties and Applications in Biomedical Fields. Journal of Macromolecular Science Part C: Polymer Reviews,32(1), 1-34.

Mukai H., Hirose A., Motai .S, Kikuchi R., Tanoi K., Nakanishi T. M., Yaita T., Kogure T. 2016. Cesium adsorption/desorption behavior of clay minerals considering actual contamination conditions in Fukushima. Nature Science Reports, 6, 21543

Muuri E., Ikonen J., Matara-aho M., Lindberg A., Holgersson S., Voutilainen M., Siitari-Kauppi M., Martin A. 2016. Behavior of Cs in Grimsel granodiorite: sorption on main minerals and crushed rock. Radiochimica Acta, AOP. doi: DOI 10.1515/ract-2016-2574

Muuri E, Siitari-Kauppi M, Matara-aho M, Ikonen J, Lindberg A, Qian L, Koskinen L .2017. Cesium sorption and diffusion on crystalline rock: Olkiluoto case study. J.Radioanal. Nuc. Ch., 311 (1): 439-446

Mäder U., Jenni A., Lerouge C., Gaboreau S., Miyoshi S., Kimura Y., Cloet V., Fukaya M., Claret F., Otake T., Shibata M., Lothenbach B. 2017. 5-year chemico-physical evolution of concrete-claystone interfaces, Mont Terri rock laboratory (Switzerland). Swiss Journal of Geosciences, 110(1), 307-327.

Möri A., Mazurek M., Adler M., Schild M., Siegesmund S., Vollbrecht A., Ota K., Ando T., Alexander W.R., Smith P.A., Haag P., Bühler Ch. 2003. Grimsel test Site Investigation Phase IV (1994-1996). The Nagra-JNC in situ study of safety relevant radionuclide retardation in fractured crystalline rock. IV: The in situ study of matrix porosity in the vicinity of a water conducting fracture. Technical Report 00-08, Nagra.

Noiriel C. 2015. Resolving Time-dependent Evolution of Pore-scale Structure, Permeability and Reactivity using X-ray microtomography. Reviews in Mineralogy and Geochemistry, 80, 247-285.

Noiriel C., Steefel C.I., Yang L., Bernard D. 2016. Effects of pore-scale precipitation on permeability and flow. Advances in Water Resources, 95, 125-137.

Norton D. & Knapp R. 1977. Transport phenomena in hydrothermal systems: the nature of porosity. American Journal of Science, 277, 913-936.

NUMO. Safety of the Geological Disposal Project 2010 – Safe Geological Disposal Based on Reliable Technologies. English Summary. Technical Report NUMO-TR-13-05.

Odian G. 2004. Principles of Polymerization. 4th edition. Wiley Interscience, Hoboken, USA.'

Ogiyama S., Suzuki H., Inubushi K., Takeda H., Uchida S. 2009. Root-uptake of 14C derived from acetic acid by root vegetables. Radioprotection, 44 (5), 365-369.

Ohkubo T., Ibaraki M., Tachi Y., Iwadate Y. 2016. Pore distribution of water-saturated compacted clay using NMR relaxometry and freezing temperature depression; effects of density and salt concentration. Applied Clay Science, 123, 148-155.

ONDRAF/NIRAS. 2011. Waste plan for the long-term management of conditioned high-level and/or long-lived radioactive waste and overview of related issues. Report NIROND 2011-02 E.

Palacios J.M., Niehoff D.L., Kuhar M.J. 1981. Receptor autoradiography with tritium-sensitive film: potential for computerized densitometry. Neuroscience Letters, 25, 101-105.

Palut J.-M., Montarnal Ph., Gautschi A., Tevissen E., Mouche E. 2003.Characterisation of HTO diffusion properties by an in situ tracer experiment in Opalinus clay at Mont Terri. Journal of Contaminant Hydrology, 61, 203-218.

Parneix J.-C., Robinet J.-C., Siitari-Kauppi M., Bouchet A., Mazurier A., Prêt D., Sammartino S. 2012 Multiscale approach for comparison of spatial distribution of porosity and mineralogy in clay rocks: examples from Boda (Hungary), Boom (Belgium), and Opalinus (Switzerland). Unpublished manuscript.

Pearson, F.J., Arcos D., Bath A., Boisson J.-Y., Fernández A.M., Gäbler H.-E., Gaucher E., Gautschi A., Griffault L., Hernán P., Waber H.N. 2003. Mont Terri project — Geochemistry of water in the Opalinus clay formation at the Mont Terri rock laboratory. Reports of the FOWG, Geology Series, no 5, Bern.

Petford N. & McCaffrey (eds.) 2003. Hydrocarbons in Crystalline Rocks, 214, 93-107.

Posiva. 2012. Safety Case for the Disposal of Spent Nuclear Fuel at Olkiluoto – Synthesis 2012. Posiva Report 2012-12. (ISBN: 978-951-652-193-3).

Posiva. 2014a.Safety Case for the Disposal of Spent Nuclear Fuel at Olkiluoto. FEP Screening and Processing. Posiva report 2014-03, Posiva Oy.

Poteri A., Nordman H., Pulkkanen V.-M., Smith P. 2014. Radionuclide transport in the Repository Near-Field and Far-Field.

Prêt D., Sardini P., Beaufort D., Zellagui R., Sammartino S. 2004. Porosity distribution in a clay gouge by image processing of C-14-PolyMethylMethAcrylate (C-14-PMMA) autoradiographs:

Case study of the fault of St. Julien 8Basin of Lodève, France). Applied Clay Science, 27, 107-118.

Priya Dasan K. 2015. Nanoclay/polymer composites: recent development and future prospects. Advanced Structured Materials, 75, 561-579.

Putnis A. 2015. Transient Porosity Resulting from Fluid-Mineral Interaction and its Consequences. Reviews in Mineralogy & Geochemistry, 80, 1-23.

Pyrak-Nolte L.J., Montemagno C.D., Yang G., Cook N.G.W., Myer L.R. 1995. Three-dimensional tomographic visualization of natural fracture networks and graph theory analysis of the transport properties. International Society for Rock Mechanics Proceedings, 8th International Conference on Rock Mechanics, Tokyo, 1995, 855-859.

Pyrak-Nolte L.J., Montemagno C.D., Nolte D.D. 1997. Volumetric imaging of aperture distributions in connectd fracture networks. Geophysical Research Letters, 24(18), 2343-2346.

Que M. & Allen A.R. 1996. Sericitization of plagioclase in the Rosses Granite Complex, Co. Donegal, Ireland. Mineralogical Magazine, 60, 927-936.

Robert R., Sardini P., Sammartino S., Dubois C., Guillot L., Rossy M., Gaviglio P., Siitari-Kauppi M. 2003. Porosity changes in a granite close quarry faces: identification from C-14-PMMA autoradiographs and mineralogical cartographies. European Physical Journal: Applied Physics, 21, 127-136.

Robinet J.-C., Sardini P., Siitari-Kauppi M., Prêt D., Yven B. 2015. Upscaling the porosity of the Callovo-Oxfordian mudstone from the pore scale to the formation scale; insights from the 3H-PMMA autoradiography technique and SEM BSE imaging. Sedimentary Geology, 321, 1-10.

Rodgers B.A. 2004. The Archaeologist's manual for conservation – A guide to non-toxic, minimal intervention artefact stabilization. Springer Science + Business Media, Inc. New York, USA. ISBN: 0-306-48613-X.

Rogers A.W. 1967. Techniques of autoradiography. Elsevier Publishing Company, Netherlands.

Rufer D. & Preusser F. 2009. Potential of autoradiography to detect spatially reseolved radiation patterns in the context of trapped charge dating. Geochronometria, 34, 1-13.

Sahlstedt E., Karhu J., Rinne K. 2014. Fracture Mineral Investigations at Olkiluoto in 2010: Implications to Paleohydrogeology. Posiva Working Report 2012-94. Posiva.

Sammaljärvi J., Lindberg A., Ikonen J. Voutilainen M., Siitari-Kauppi M., Koskinen L. 2014. Investigation of mineralogy, porosity and pore structure of Olkiluoto bedrock. Material Research Society Symposium Proceedings. 1665, 31-37.

Sammaljärvi J., Ikonen J., Voutilainen M., Kekäläinen P., Lindberg A., Siitari-Kauppi M., Pitkänen P., Koskinen L. 2017. Chloride diffusion in pore water in Olkiluoto veined gneiss and pegmatitic granite from a structural perspective. MRS Advances, 1 (61), 2047-4052.

Sammartino S., Siitari-Kauppi M., Meunier A., Sardini P., Bouchet A., Tevissen E. 2002. An imaging method for the porosity of sedimentary rocks: adjustment of the PMMA method – Example of a characterization of a calcareous shale. Journal of Sedimentary Research, 72 (6), 937-943.

Sammartino S., Bouchet A., Prêt D., Parneix J.-C., Tevissen E. 2003. Spatial distribution of porosity and minerals in clay rocks from the Callovo-Oxfordian formation (Meuse/Haute-Marne, Eastern France) – implications on ionic species diffusion and rock sorption capability. Applied Clay Science, 23, 157-166.

Sardini P., Siitari-Kauppi M., Beaufort D., Hellmuth K.-H. 2006. On the connected porosity of mineral aggregates in crystalline rocks. American Mineralogist, 91, 1069-1080.

Sardini P., Kuva J., Siitari-Kauppi M., Hellmuth K.-H. 2014. A simplified simulation approach for estimating crack aperture using ^{14}C-PMMA method. 2014. Journal of Coupled Systems and Multiscale Dynamics, 2(4), 244-255.

Sardini P., Caner L., Mossler P., Mazurier A., Hellmuth K.-H., Graham R.C., Rossi A.M., Siitari-Kauppi M. 2015. Calibration of digital autoradiograph technique for quantifying rock porosity using C-14-PMMA method. Journal of Radioanalytical and Nuclear Chemistry, 303, 11-23.

Sardini P., Angileri A., Descostes M., Duval S., Oger T., Patrier P., Rividi N., Siitari-Kauppi M., Toubon H., Donnard J. 2016. Quantitative autoradiography of alpha particle emission in geo-materials using the Beaver system. Nuclear Instruments and Methods in Physics Research A, 833, 15-22.

Scrivener K.L., Füllmann T., Gallucci E., Walenta G., Bermejo. 2004. Quantitative study of Portland cement hydration by X-ray diffraction/Rietveld analysis and independent methods. Cement and Concrete Research, 34(9), 1541-1547.

Sevee J.E. 2010. Effective Porosity Measurement of a Marine Clay. Journal of Environmental Engineering, 136(7), 674-681.

SFOE (Swiss Federal Office of Energy). 2008. Sectoral Plan for Deep Geological Repositories – Conceptual Part. English Translation, published on 2.4.2008.

Siitari-Kauppi M., Flitsiyan E.S., Klobes P., Meyer K., Hellmuth K-H. (1998). Progress in physical rock matrix characterization: structure of the pore space. In: I.G. McKinley, C. McCombie (edits.), Scientific Basis for Nuclear Waste Management XXI, Mat. Res. Soc. Symp. Proc. 506, 671-678.

Siitari-Kauppi M., Hölttä P., Pinnioja S., Lindberg A. 1999. Cesium sorption on tonalite and mica gneiss. Material Research Society Symposium Proceedings. 556, 1099-1106.

Siitari-Kauppi M. 2002. Development of C-14-polymethylmethacrylate method for the characterisation of low porous media – Application to rocks in geological barriers of nuclear waste storage. Academic Dissertation. Report Series in Radiochemistry, 17/2002.

Skagius K & Neretnieks I. 1985. Porosities and diffusivities of some non-sorbing species in crystalline rocks. SKB Technical report TR-85-03. SKB.

SKB. 2010a. Choice of method – evaluation of strategies and systems for disposal of spent nuclear fuel. SKB Report P-10-47. ISSN: 1651-4416.

SKB. 2010b. Design and production of the KBS-3 repository. SKB Report TR-10-12. ISSN: 1404-0344.

Smellie (ed.), Pitkänen P., Koskinen L., Aaltonen I., Eichinger F., Waber N., Sahlstedt E., Siitari-kauppi M., karhu J., Löfman J., Poteri A., 2014. Evolution of the Olkiluoto site: Paleohydrogeochemical considerations. Posiva working report 2014-27.

Smith D., Pivonka P., Jungnickel C., Fityus S. 2004. Theoretical analysis of anion exclusion and diffusive transport through platy-clay soils. Transport in Porous Media, 57, 251-277

Soeder D.J. 1990. Applications of Fluorescence Microscopy to Study of Pores in Tight Rocks. AAPG Bulletin, 74(1), 30-40.

Soler J.P., Landa J., Havlova V., Tachi Y., Ebina T., Sardini P., Siitari-Kauppi M., Eikenberg J., Martin A.J. 2015. Comparative modeling of an in situ diffusion experiment in granite at the Grimsel Test Site. Journal of Contaminant Hydrology, 179, 89-101.

Solon E.G., Schweitzer A., Stoeckli M., Prideaux B. 2010. Autoradiography, MALDI-MS, and SIMS-MS Imaging in Pharmaceutical Discovery and Development. The AAPS Journal, 12(1), 11-26.

Solon E.G. 2015. Autoradiography techniques and quantification of drug distribution. Cell Tissue Research. 360, 87-107.

Sprunt E V & Brace W F (1974) Direct observation of microcavities in crystalline rocks, International Journal of Rock Mechanics and Mining Sciences. 11, 139-150.

Stack A.G. 2015. Precipitation in Pores: A Geochemical Frontier. Reviews in Mineralogy & Geochemistry, 80, 165-190.Swift P.N. & Bonano E.J. 2015. Geological Disposal of Nnuclear Waste in Tuff: Yucca Mountain (USA). Elements, 12, 263-268.

Thompson J.L. & Wolfsberg K. 1979. Applicability of Microautoradiography to Sorption Studies. LA-7609-MS Informal Report. Los Alamos Scientific Laboratories.

Toropainen V. 2012. Core drilling of REPRO drillholes in ONKALO at Olkiluoto 2010-2011. Posiva working report 2012-26. Posiva.

Treutler H.C. & Freyer K. 1985. On problems of standardized handling and quantitative evaluation of autoradiograms. 14th International Symposium on Autoradiography, 19-23.11.1984, Reinhardsbrunn, GDR.

Tsai T.-Y., Lin M.-J., Chang C.-W., Li C.-C. 2010. Morphology and properties of poly(methyl methacrylate)&clay nanocomposites by in-situ solution polymerization. Journal of Physics and Chemistry of Solids, 71, 590-594.

Unnerstall J.R., Niehoff D.L., Kuhar M.J., Palacios J.M. 1982. Quantitative receptor autoradiography using[^{3}H]Ultrofilm: application to multiple benzodiazepine receptors. Journal of Neuroscience Methods, 6, 59-73.

Uusinoka R. 1983. Rapautumisilmiöt kallioperässä. Rapautuminen kallioperässä symposium, 9.11.1983, Espoo. Papers of the Engineering Geological Society of Finland, 15, 1-28. (in Finnish).

Van Loon L. C., Glaus M. A., Müller W. 2007. Anion exclusion effects in compacted bentonites: Towards a better understanding of anion diffusion. Applied Geochemistry 22, 2536-2552.

Velde B., Meunier A. 2008. The Origin of Clay Minerals in Soils and Weathered Rocks. Springer, Germany. (ISBN: 978-3-540-75633-0)

Vogel, A.I., 1985. A Textbook of Quantitative Inorganic Analysis; Including Elementary Instrumental Analysis, Third Edition, London, pages 740-742.

Voutilainen M., Lamminmäki S., Timonen J., Siitari-Kauppi M., Breitner D. 2009. Physical rock matrix characterization: structural and mineralogical heterogeneities in granite. Material Research Society Symposium Proceedings, 1124.

Voutilainen M. 2012. Characterisation of structure and diffusion in geological materials. Academic dissertation for the degree of Doctor of Philosophy. Department of Physics, University of Jyväskylä. Research Report 12/2012.

Voutilainen M., Siitari-Kauppi M., Sardini P., Lindberg A., Timonen J. 2012. Pore-space charaterization of an altered tonalite by X-ray computed microtomography and the C-14-labeled-polymethylmethacrylate method. Journal of Geophysical Research, 117, B01201.

Voutilainen M., Sardini P., Siitari-Kauppi M., Kekäläinen P., Aho V., Myllys M., Timonen J. 2013. Diffusion of Tracer in Altered Tonalite: Experiments and Simulations with Heterogeneous distribution of porosity. Transport in Porous Media. 96, 319-336.

Voutilainen M, Poteri A, Helariutta K, Siitari-Kauppi M, Nilsson K, Andersson P, Byegård J, Skålberg M, Kekäläinen P, Timonen J, Lindberg A, Pitkänen P, Kemppainen K, Liimatainen J, Hautojärvi A, Koskinen L 2014. In-situ Experiments for Investigating the Retention Properties of Rock Matrix in ONKALO, Olkiluoto, Finland – 14258. Waste Management Conference, March 2-6 2014, Phoenix, Arizona, USA.

Voutilainen M., Ikonen J., Sammaljärvi J., Kuva J. Lindberg A., Siitari-Kauppi M., Koskinen L. 2017a. Through diffusion study on Olkiluoto veined gneiss and pegmatitic granite from a structural perspective. MRS Advances. 1(61), 4041-4046.

Voutilainen M., Kekäläinen P., Kuva J., Siitari-Kauppi M., Yli-Kaila M., Koskinen L. 2017b. Laboratory scale advection-matrix diffusion experiment in Olkiluoto veined gneiss using H-3 and Cl-36 as tracers. MRS Advances. 2(12), 655-660.

Walsh Z., Janecek E.-M., Hodgkinson J.T., Sedlmair J., Koutsioubas A., Spring D.R., Welch M., Hirschmmugl C.J., Toprakcioglu C., Nitschke J.R., Jones M., Scherman O.A. 2014. Multifunctional supramolecular polymer networks as next-generation consolidants for archaeological wood conservation. Proceedings of the National Academy of Sciences. 111(50).

Walsh Z., Janecek E.-M., Jones M., Scherman O.A. 2017. Natural polymers as alternative consolidants for the preservation of waterlogged archaeological wood. Studies in Conservation, 62(3).

Wang D., Zhu J., Yao Q., Wilkie C.A. 2002. A comparison of various methods for the preparation of polystyrene and poly(methyl methacrylate) clay nanocomposites. Chemistry of Materials, 14, 3837-3843.

Wang R., Pavlin T., Rosen M.S., Mair R.W., Cory D.G., Walsworth R.L. 2005. Xenon NMR measurements of permeability and tortuosity in reservoir rocks. Magnetic Resonance Imaging, 23, 329-331.

Widestrand H, Byegård J, Cvetkovic V, Tullborg E-L, Winberg A, Andersson P, Siitari-Kauppi M (2007) Sorbing tracer experiments in crystalline rock fracture at Äspö (Sweden): 1, Experimental setup and microscale characterization of retention properties. Water Resources Research 43:W10413.

Widestrand H, Byegård J, Selnert E, Skålberg M, Höglund S, Gustafsson E. 2010. Long Term Sorption Diffusion Experiment (LTDE-SD). Supporting laboratory program – Sorption diffusion experiments and rock material characterisation. With supplement of adsorption studies on intact rock samples from the Forsmark and Laxemar site investigations. SKB Report R-10-66, SKB.

Williams D.H., Fleming I. 1995. *Spectroscopic methods in organic chemistry*. 5th edition. McGraw Hill, Glasgow.

Willis K.L., Abell A.B., Lange D.A. Image-based characterization of cement pore structure using Wood's metal intrusion. Cement and Concrete Research, 28(12), 1695-1705.

Woods, R.J. and Pikaev A.K., 1994. Applied Radiation Chemistry: Radiation Processing, John Wiley & Sons, New York, 352-354

Zeng C., Lee L.J. 2001. Poly(methyl methacrylate) and Polystyrene/Clay nanocomposites prepared by in-situ polymerization. Macromolecules, 34, 4098-4103.

Zhang W., Li Y., Wei L., Fang Y. 2003. In situ intercalative polymerization of poly(methyl methacrylate)/clay nanocomposites by γ-ray irradiation. Materials Letters, 57, 3366-3370.

Zinszner B. & Pellerin F.M. 2007. A Geoscientist's guide to petrophysics. IFP Publications. ISBN-10: 2710808994